


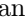




Co-Designing Eigen- and Singular-value Transformation Oracles: From Algorithmic Applications to Hardware Compilation

Luke Bell ^{1,2,*} Yan Wang ^{3,†} Kevin C. Smith ^{4,5,1,‡}
Yuan Liu ^{6,7,8} Eugene Dumitrescu ^{3,§} and S. M. Girvin ^{1,5}

¹*Department of Physics, Yale University, New Haven, Connecticut 06520, USA*

²*Department of Physics, University of California Santa Barbara, Santa Barbara, California 93106, USA*

³*Computational Sciences and Engineering Division, Oak Ridge National Laboratory, Oak Ridge, Tennessee 37831, USA*

⁴*Brookhaven National Laboratory, Upton, New York 11973, USA*

⁵*Yale Quantum Institute, Yale University, New Haven, Connecticut 06520-8263, USA*

⁶*Department of Electrical and Computer Engineering, North Carolina State University, Raleigh, North Carolina 27606, USA*

⁷*Department of Computer Science, North Carolina State University, Raleigh, North Carolina 27606, USA*

⁸*Department of Physics, North Carolina State University, Raleigh, North Carolina 27606, USA*

(Dated: May 22, 2025)

We co-design a family of quantum eigenvalue transformation oracles that can be efficiently implemented on hybrid discrete/continuous-variable (qubit/qumode) hardware. To showcase the oracle's representation-theoretic power and near-term experimental accessibility, we encode a Gaussian imaginary time evolution spectral filter. In doing so, we define a continuous linear combination of unitaries block-encoding. Due to the ancilla qumode's infinite-dimensional nature, continuous variable qumodes constitute a powerful compilation tool for encoding continuous spectral functions without discretization errors while minimizing resource requirements. We then focus on the ubiquitous task of eigenstate preparation in quantum spin models. For completeness, we provide an end-to-end compilation—applicable in both near-term and large-scale quantum processors—expressing high-level oracles in terms of an experimentally realizable instruction set architecture. Our algorithms scale linearly with the spatial extent of the target system, and we provide details for 1D and 2D examples. Finally, we examine the leading-order effects of physical errors and highlight open research directions.

CONTENTS

I. Introduction	2	III. Hardware Architecture and Compilation	6
II. Methods	2	A. Layout and Connectivity	6
A. Gaussian Imaginary Time Evolution	3	B. CV-DV Compilation	6
B. Block Encoding Eigenvalue Transformation Oracles	3	IV. Heisenberg Model Compilation	7
1. Continuous Linear Combination of Unitaries	3	A. Synthesizing Time-Evolution	7
2. Controlled Displacements and Measurement	4	B. 2-Local Gadget	8
C. Generalized Integral Transformations Oracles	5	C. Parallelizing Compilation in 1D	9
		1. One-Oscillator Compilation	9
		2. Two-Oscillator Compilation	9
		D. Multi-Oscillator Compilation	10
		E. 1D SWAP Networks	11
		F. Numerical Results	12
		1. $\alpha \ll 1$ LTPF Regime	12
		2. $\alpha \gg 1$ Floquet-Regime	14
		3. Optimization	14
		G. Algorithm in 2D	15
		V. Physical Error Analysis	16
		VI. Conclusion	17
		Acknowledgments	17
		A. Brief review of continuous variables	18
		B. Proof of Theorem 5	19
		C. Analytical Results for 1D Chain	20

This manuscript has been authored by UT-Battelle, LLC, under Contract No. DE-AC0500OR22725 with the U.S. Department of Energy. The United States Government retains and the publisher, by accepting the article for publication, acknowledges that the United States Government retains a non-exclusive, paid-up, irrevocable, worldwide license to publish or reproduce the published form of this manuscript, or allow others to do so, for the United States Government purposes. The Department of Energy will provide public access to these results of federally sponsored research in accordance with the DOE Public Access Plan.

* lukebell@ucsb.edu

† wangy2@ornl.gov

‡ Present address: IBM Quantum, Cambridge, MA

§ dumitrescuef@ornl.gov

I. INTRODUCTION

How much algorithmic and physical co-design is required to establish near-term quantum computational advantage? From a computer science perspective, one must compile broad classes of opaque quantum oracles, such as general singular-value transformations [1, 2] and eigenvalue filters [3]. From an experimental and co-design perspective, one wishes to judiciously leverage particular physical features to minimize the total hardware resources required. For example, expanding the compilation space from qubit to qudit on mixed-radix superconducting hardware, was shown to minimize the total effective gate cost [4].

Quantum harmonic oscillators, or qumodes [5], are a manifestly continuous quantum computational type that are ancillary degrees of freedom already implicitly used in compiling two-body, or multi-qubit, entangling gates, e.g., on trapped ion machines [6–8]. For simple lattice gauge theories, recent works show how to natively encode and promote force carriers to first-class (native) quantum types [9, 10]. Mathematically, qumodes are fundamentally different from finite-dimensional qudits due to their infinite, rather than finite, Hilbert space dimension. It has therefore been conjectured that qumode quantum registries could radically expand computational capabilities [11]. Using a continuous variable ancilla, reference [12] develops a quantum algorithm to prepare quantum spin systems at finite temperatures. However, end-to-end hardware compilation strategies for many-body interacting models are required.

We focus here on an architecture which comprises a lattice of continuous variable (CV) oscillators and a dual lattice of discrete variable (DV) qubits. A physical hardware realization, with all necessary native gates and the connectivity used in our co-design, is provided by a lattice of superconducting cavities and transmon qubits [13–15]. Within this setting, we propose a constructive algorithm for CV-controlled time-evolution oracles filtering the spectral weight of spin- $\frac{1}{2}$ (qubit) systems with respect to a target Hamiltonian. Utilizing a concrete instruction set architecture (ISA) [15], our main result is the end-to-end compilation of a singular-value transformation oracle spectrally filtering quantum spin chains.

By showing how continuous variables go beyond simulating bosons, our protocol emphasizes the algorithmic utility of the oscillators in compilations which now concretely represent a powerful tool for resource-efficient quantum signal analysis. To show how our formalism efficiently compiles subroutines that usually lack efficient (or even explicit) implementations, we provide concrete algorithms for eigenstate preparation based on Gaussian filtering. By compiling continuous transformations

with CV environmental degrees of freedom, our proposed quantum imaginary time evolution (QITE) simultaneously minimizes hardware resource requirements, saturates optimality bounds, and is embarrassingly parallelizable.

To provide intuition for our algorithm, Sec. II outlines how infinite-dimensional bosonic modes constitute a powerful resource for efficiently expressing and compiling block-encoded operations in quantum algorithms. Then, combining a native qubit-Hamiltonian/qumode-displacement unitary with measurement on the ancillary qumode registry, we synthesize a family of continuous eigenvalue transformation oracles. We note that the individual quantum operations necessary for our approach – qubit conditioned oscillator displacements followed by high-fidelity measurement of the boson number – were efficiently performed in recent experiments using boson sampling to simulate Franck-Condon factors in triatomic molecules [16] and simulating molecular dynamics near a conical intersection [17].

Next, in Section III, we proceed to highlight the key role qubit-controlled oscillator displacements [15] play in efficiently encoding spectral filters. We then describe hardware layout, physical instruction sets, and the subsequent compilation schemes co-designed with regard to the former. Section IV then provides the protocol for eigenstate preparation of the Heisenberg spin chain, including a theory of imaginary-time Trotter error. Finally, Sec. V analyzes leading-order physical errors before we conclude in Sec. VI with a discussion of next steps and open problems.

II. METHODS

To begin, Sec. II A constructs spectral projectors from continuous linear superpositions of time evolutions. Section II B then presents the complex-time evolution oracle as a controlled displacement oracle in a hybrid CV-DV system. By considering continuous and discrete CV measurements, Section II C further generalizes the spectral and singular-value filters to those with Hamiltonian-Hermite polynomials or additional real-time evolutions.

Before delving into the technical details, we present here an informal and high-level outline of the scheme. For pedagogical purposes, let us consider for now only a single qumode which can interact with a spin chain via a series of hybrid qubit-qumode gates. Let the input state of the spin chain be a superposition of energy eigenstates, and let the qumode be in the vacuum (ground) state,

$$|\Psi_{\text{in}}\rangle = \sum_n \psi_n |E_n\rangle \otimes |0\rangle. \quad (1)$$

The basis of our protocol is a circuit (to be described in detail later) in which the qumode is sent into a coherent state $|\alpha\rangle$ displaced in position from the origin by a distance proportional to the energy of the spin chain.

Ideally, the protocol maps the initial state to

$$|\Psi_{\text{out}}\rangle = \sum_n \psi_n |E_n\rangle \otimes |\alpha_n\rangle, \quad (2)$$

where $|\alpha_n\rangle$ is a qumode coherent state with amplitude proportional to the n th energy eigenvalue of the spin system $\alpha_n = \alpha(E_n - E_s)$, with the constant α being dependent on the details of the circuit, and the energy offset E_s being set by the user. The final step is to measure the photon number in the qumode, post-selecting on obtaining zero. The measurement disentangles the spin chain from the oscillator, leaving the oscillator in the final state

$$|\Psi_{\text{final}}\rangle \propto \sum_n \psi_n |E_n\rangle \langle 0|\alpha_n\rangle, \quad (3)$$

where we have ignored the normalization factor. Upon measuring the qumode to be in the vacuum state, Gaussian energy filtering arises from the overlap $\langle 0|\alpha_n\rangle = \exp(-|\alpha_n|^2/2)$. We turn now to a more detailed discussion of the circuit needed to realize this filtering process and how to compile it using an experimentally realistic instruction set.

A. Gaussian Imaginary Time Evolution

Given a target Hamiltonian \hat{H} , denote its eigenenergy-eigenvector pairs, in the order of ascending energy, as $\{(E_n, |E_n\rangle)\}_{n=0}^N$. A spectrum-shifted Hamiltonian $\hat{H}' = \hat{H} - E_s$, has the same eigenstates as \hat{H} . When shifting by the ground state energy, $E_s := E_0$, the generator \hat{H}' is positive semidefinite $\hat{H}' \geq 0$, meaning that its spectrum is non-negative. For the remainder of the article for simplicity, we assume a closed ($E_s \in \mathbb{R}$) principal system. Define a Gaussian QITE propagator:

$$\hat{P}_{\hat{H}'}(\tau) = e^{-\frac{1}{2}\hat{H}'^2\tau^2} = \sum_n e^{-\frac{1}{2}(E_n - E_s)^2\tau^2} |E_n\rangle\langle E_n| \quad (4)$$

$$= |E_0\rangle\langle E_0| + \sum_{n \neq 0} e^{-\frac{1}{2}(E_n - E_0)^2\tau^2} |E_n\rangle\langle E_n|. \quad (5)$$

Equation (4) indicates $\hat{P}_{\hat{H}'}(\tau)$ filters a quantum state by Gaussian weights, centered around E_s , on its components in terms of the Hamiltonian eigenbasis (common basis for both \hat{H} and \hat{H}'). In Eq. (5) $E_s := E_0$. If $E_n > E_0$ for all $n \neq 0$, meaning the shift is with respect to a non-degenerate ground state [18]), and in the limit $\tau \rightarrow \infty$, $\hat{P}_{\hat{H}'}(\tau \rightarrow \infty) = |E_0\rangle\langle E_0|$ becomes a ground state projector. In the same limit but with $E_s := E_n$, we obtain an eigenstate projector $|E_n\rangle\langle E_n|$, while for arbitrary E_s it results in an energy filter near E_s . Recent works investigated iteratively learning E_0 when it is a-priori unknown [19].

Instead of naively compiling Eq. (4) in terms of an exponential of the unwieldy generator \hat{H}'^2 , we simplify

compilation with the Hubbard-Stratonovich (HS) integral transformation. Begin with the Gaussian integral identity $\mathbb{1} = \sqrt{a/\pi} \int dp \exp[-a(p\mathbb{1} + \hat{K})^2]$, where $\text{Re } a \geq 0$ for $a \neq 0$, \hat{K} is any operator, and $\mathbb{1}$ is the corresponding identity operator. Multiplying both sides of the Gaussian integral identity with $e^{a\hat{K}^2}$ results in

$$e^{a\hat{K}^2} = \sqrt{\frac{a}{\pi}} \int_{-\infty}^{+\infty} dp e^{-ap^2} e^{-2a\hat{K}p}. \quad (6)$$

The next step is to interpret Eq. (6) as a HS integral transformation encoding of Eq. (5)'s QITE propagator in terms of a *continuous* linear combination of unitaries. To see this, select $\hat{K} = -i\hat{H}'\tau/2$ and define tensor product space time evolution operators as

$$U_{\hat{Q}}^{(\hat{B})}(t) \equiv e^{-i2t\hat{B} \otimes \hat{Q}}. \quad (7)$$

Then, letting $\mathcal{N}(\mu, \sigma)$ denote a normal distribution and setting $a = 2$ (see Appendix A), we arrive at

$$\hat{P}_{\hat{H}'}(\tau) = \sqrt{\frac{2}{\pi}} \int_{-\infty}^{+\infty} dp e^{-2p^2} e^{-2i\tau\hat{H}'p} \quad (8)$$

$$= \int_{-\infty}^{+\infty} dp \mathcal{N}(0, 1/2) U_{\hat{H}'}^{(p)}(\tau). \quad (9)$$

The next section outlines how compilation in terms of CV/DV real-time evolution unitaries and bosonic measurements is more resource-efficient than factorizing the QITE propagator directly in the qubit's Hilbert space.

B. Block Encoding Eigenvalue Transformation Oracles

Quantum mechanical operations are required to realize Eq. (8) as a circuit. The first component is a unitary and controlled interaction between the ancilla qumode and principal system. The second component is the ability to initialize the ancilla CV system into the vacuum state $|n=0\rangle$, as well as to measure the projector onto the $|n=0\rangle\langle n=0|$ state. Let us now examine how such initializations, unitaries, and measurements serve to define families of nonunitary, block-encoded operators spectrally filtering the principal system.

1. Continuous Linear Combination of Unitaries

Recently, an ε -approximation of \hat{P}_τ was proposed [20] (for qubit-only hardware) in the context of the linear combinations of unitaries (LCU) block-encoding method [21]. This work matched the asymptotically optimal, qubitization-based, bounds from earlier Refs. [19, 22] which also handle algorithmic and discretization errors within a DV setting. Alternatively, near-term $e^{-\tau H}$, QITE strategies have been investigated. Ref. [23] and

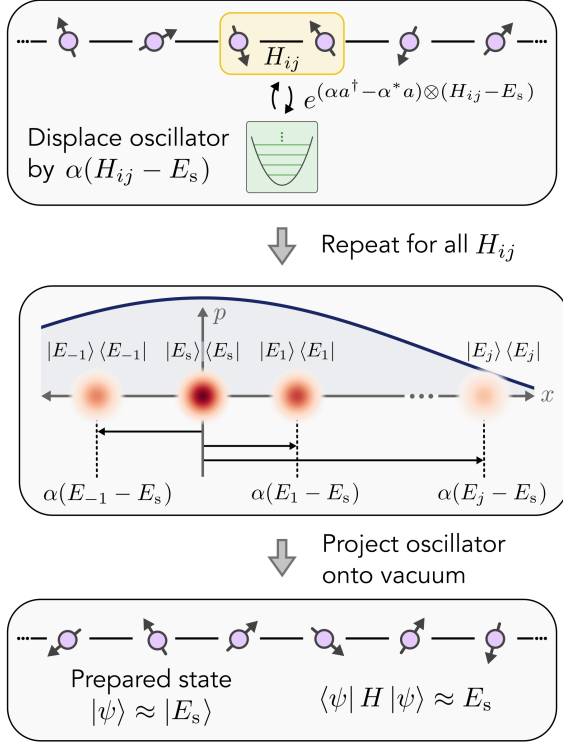


FIG. 1. Top panel: Schematic illustration of a displacement α controlled on a local interaction H_{ij} . Middle panel: The spin spectrum decays as a result of spectrum-conditioned oscillator translations and measurement which results in the bottom panel's approximate ground state.

follow-on works suggest finding the shortest depth unitary minimizing the ε -error from a target QITE. However, applying this approach to genuine many-body systems generically suffers from exponential resource costs stemming from either the original tomography or later derivative-based variational methods [24].

Block-encoding is a powerful tool for encoding general purpose, non-unitary operations [1, 2] within quantum computations. An efficient realization of block-encodings is crucial for achieving general purpose linear-algebraic advantages, e.g., in quantum singular transform-based algorithms. It has previously been shown that discrete-variable quantum resources (ancillary qubits) can be used to construct efficient block-encodings of both DV [25–27] and CV operators [15, 28, 29]. By “bosonizing” the continuous linear combination of unitaries oracle, we simultaneously remove discretization errors and minimize the ancillary resources required by effectively carrying out the Gaussian integral exactly rather than approximating it by a Riemann sum. Further, the non-trivial **Prepare** and **Select** circuits are dramatically simplified into a single continuous-variable gate which, without loss of generality, we synthesize in Sec. III. We now detail a particular hybrid architecture which consists of i) a qubit-sub-lattice and ii) a qumode-sub-lattice. The *native* in-

teractions between the pair of sub-lattices are denoted by pairs of arrows in the top panel of Fig. 1.

Note Eq. (8) can be encoded by a *single* ancillary qumode. This is because the CV, first quantized dimensionless position $\hat{x} := \frac{1}{2}(a + a^\dagger)$ and momentum $\hat{p} := \frac{i}{2}(a^\dagger - a)$ operators obey the canonical commutation relation (CCR) $[\hat{x}, \hat{p}] = (i/2)\mathbb{1}$ [30] and have continuous eigen-spectrum $x, p \in \mathbb{R} = (-\infty, \infty)$ [31]. The operators \hat{a}^\dagger and \hat{a} are the bosonic creation and annihilation operators (see Appendix A for more details) for a photon of a superconducting circuit cavity’s electromagnetic mode or a phonon of a mechanical vibration mode. Representing Eq. (8) on a single qumode will enable us to later parallelize QITE and reduce the required resources.

Before entangling with DV qubits, recall the j^{th} qumode’s (unconditional) displacement gate [15]:

$$D^{(j)}(\alpha) = e^{\alpha \hat{a}_j^\dagger - \alpha^* \hat{a}_j} \equiv e^{\tilde{\alpha}_j} \quad (10)$$

$$= e^{\alpha \hat{a}_j^\dagger} e^{-\alpha^* \hat{a}_j} e^{-|\alpha|^2/2} \quad (11)$$

$$= e^{2i[(-\text{Re } \alpha)\hat{p}_j + (\text{Im } \alpha)\hat{x}_j]}$$

$$= e^{-2i(\text{Re } \alpha)\hat{p}_j} e^{2i(\text{Im } \alpha)\hat{x}_j} e^{i(\text{Re } \alpha)(\text{Im } \alpha)}$$

$$= D^{(\hat{p}_j)}(\text{Re } \alpha) D^{(\hat{x}_j)}(i \text{Im } \alpha) e^{i(\text{Re } \alpha)(\text{Im } \alpha)}. \quad (12)$$

Coherent states are then defined as phase-space displacements $|\alpha\rangle \equiv D(\alpha)|0\rangle$. While usually defined in terms of the anti-Hermitian generator $-2i\alpha\hat{p}_j \equiv \alpha\hat{a}_j^\dagger - \alpha^*\hat{a}_j = -2i[(\text{Re } \alpha)\hat{p}_j - (\text{Im } \alpha)\hat{x}_j]$, it is also useful to examine the Hermitian generators $2(\text{Re } \alpha)\hat{p}_j$ and $-2(\text{Im } \alpha)\hat{x}_j$. The former (latter), defined in terms of \hat{p}_j (\hat{x}_j), generates spatial (momentum) translations displacing the oscillator’s position (momentum) $\langle\alpha|\hat{x}_j|\alpha\rangle = \text{Re } \alpha$ ($\langle\alpha|\hat{p}_j|\alpha\rangle = \text{Im } \alpha$). For simplicity, and without loss of generality, we take $\alpha \in \mathbb{R}$ such that $D^{(j)}(\alpha \in \mathbb{R}) = D^{(p_j)}(\alpha) = e^{-2i\alpha\hat{p}_j}$, for the remainder of this work.

2. Controlled Displacements and Measurement

CV bosonic oscillators (indexed with superscript $j \in B$) and DV qubits (indexed with subscript $k \in Q$) are coupled in the hybrid architecture under consideration. The native entangling gate, displacing the oscillator conditioned on a qubit’s $\sigma_k^Z := Z_k$ degree of freedom, is

$$D_{Z_k}^{(j)}(\alpha) = e^{-2i\alpha Z_k \otimes \hat{p}_j}. \quad (13)$$

From a qubit perspective, Eq. (13) block-encodes a position boost $e^{-2i\alpha\hat{p}_B} = \langle 0|_Q D_{Z_Q}^{(B)}(\alpha)|0\rangle_Q$ in the upper-left block of a qubit’s $\text{SU}(2)$. Exchanging the role of qubit and the oscillator, Eq. (13) block-encodes a qubit operator within the vacuum transition amplitude (VTA) of the oscillator subspace, i.e., $\langle 0|_B D_{Z_Q}^{(B)}(\alpha)|0\rangle_B = |0\rangle_Q \langle 0|_Q \otimes \langle 0|_B e^{2i\alpha\lambda_0\hat{p}}|0\rangle_B + |1\rangle_Q \langle 1|_Q \otimes \langle 0|_B e^{-2i\alpha\lambda_1\hat{p}}|0\rangle_B = e^{-\alpha^2/2}(|0\rangle_Q \langle 0|_Q + |1\rangle_Q \langle 1|_Q)$. In this case both qubit levels

$\{|0\rangle_k, |1\rangle_k\}$ are equally projected since their energies are $\lambda_{0,1} = \pm 1$ and equal in absolute distance from $E_s = 0$.

We are now in a position to generalize Eq. (13), with a qubit-controlled translation, to a many-body-spectrum-controlled translation. A precise example is presented later in Sec. IV. By promoting single qubit $\mathfrak{su}(2)$ generators to many-body Hamiltonians, as $Z_k \rightarrow \hat{H}'$, we see:

Lemma 1 (CV-DV phase kick-back). *An oscillator position displacement weighted by the spectrum of a spin chain \hat{H}' is, by interchanging the role of spin chain and oscillator (see Fig. 1), equivalent to a real-time dynamics of \hat{H}' with the evolution time weighted by the oscillator's momentum:*

$$D_{\hat{H}'}^{(j)}(\alpha \in \mathbb{R}) := e^{-2i\alpha\hat{H}' \otimes \hat{p}_j} =: U_{\hat{H}'}^{(\hat{p}_j)}(\alpha). \quad (14)$$

We will use the left hand side expression when discussing hardware compilation and the right hand side expression in an algorithmic context. This leads to our first result:

Theorem 2 (CV-DV-HS Transformation Oracle). *The Eigenvalue Transformation Oracle in Eq. (4) can be block-encoded as a Vacuum Transition Amplitude (VTA):*

$$\langle 0|D_{\hat{H}'}^{(j)}(\alpha)|0\rangle = \int dp \langle 0|p\rangle \langle p|D_{\hat{H}'}^{(j)}(\alpha)|0\rangle, \quad (15)$$

$$= \int dp \langle 0|p\rangle \langle p|0\rangle e^{-i2\alpha p \hat{H}'} \quad (16)$$

$$= \hat{P}_{\hat{H}'}(\alpha). \quad (17)$$

Proof: Insert the momentum-space resolution of identity to derive the first line, act in the momentum basis in the second line, and use $\langle 0|p\rangle \langle p|0\rangle = (2/\pi)^{1/2} e^{-2p^2}$ (Appendix A) to encode the continuous normal distribution $\mathcal{N}(0, 1/2)$ in the last step.

Eq. (17) offers a bosonically block-encoded representation of Eq. (5). In this interpretation, the final oscillator state after the controlled displacement is a function of E_n as in the middle panel of Fig. 1. Projecting the ancillary qumode onto the vacuum state then reveals a diagonal qubit ensemble $\rho_Q = \sum_n p_n |E_n\rangle\langle E_n|$ with probability $p_n = e^{-\frac{1}{2}(E_n - E_s)^2 \alpha^2} / \sum_n e^{-\frac{1}{2}(E_n - E_s)^2 \alpha^2}$. With α and E_s parametrically tuning the filter strength and target energy, this corresponds to the Gibbs ensemble for Hamiltonian \hat{H}'^2 and the inverse temperature $\beta = \alpha^2/2$.

C. Generalized Integral Transformations Oracles

For completeness, we now highlight the extended family of block encodings appearing as vacuum to non-vacuum transition amplitudes. Recall that in a DV block encoding one prepares initial DV ancilla state $|0\rangle$ and, depending on the final measured state $|j\rangle$, has subsequently applied a (possibly non-unitary) $\hat{A}_{0,j}$. Deterministic quantum algorithms [32] typically consider only

the $j = 0$ sector. Consider first the positive operator-valued measure (POVM) $\{|m\rangle\langle m|\}$ associated with a microwave photon detector measuring the final state of the oscillator in the m -photon Fock state basis $|m\rangle$ with $m \in \{0, 1, \dots\} \equiv \mathbb{N}_0$.

Using $H_m(p)$ to denote the m th Hermite polynomial and m -photon wavefunction $\psi_m(p) = \langle p|m\rangle$ given at the end of Appendix A, we have

$$\begin{aligned} \hat{P}_{\hat{H}'}(m, \tau) &= \int_{-\infty}^{+\infty} dp \langle m|p\rangle U_{\hat{H}'}^{(p)}(\tau) \langle p|0\rangle \\ &= \frac{i^m}{\sqrt{\pi 2^{m-1} m!}} \int_{-\infty}^{+\infty} dp e^{-2p^2} H_m(\sqrt{2}p) e^{-i\hat{H}'\tau 2p} \\ &= \frac{(\tau \hat{H}')^m}{\sqrt{m!}} e^{-\frac{\tau^2}{2} \hat{H}'^2}. \end{aligned} \quad (18)$$

An additional simplified proof of Eq. (18) using operator calculus [33] appears in Eq. (A4).

The integral in the last step can be viewed as *Hermite integral transform* which reduces to the HS transform when $m = 0$. The corresponding Hermite transform pair of the time evolution oracle $e^{-it\hat{H}}$ can be looked up in a standard mathematical table. In Eq. (8), the number dependent prefactor $\langle m|z\rangle = \frac{z^m}{\sqrt{m!}} \langle 0|z\rangle$ simplified to unity. For $m = 0$, Eq. (18) reduces Eq. (4) and for $\tau = 0$ this expression reduces to the Fock-basis delta function $\langle m|0\rangle = \delta_{m,0}$. For $\tau > 0$ we complete the square and integrate. Changing to variable $p' = p + iH'\tau$, and using $H_m(p)$ to denote the m th Hermite polynomial, gives us

$$\hat{P}_{\hat{H}'}(m, \tau) = \frac{e^{-\frac{1}{2}\hat{H}'^2\tau^2}}{\sqrt{2\pi}} \int_{-\infty+i\hat{H}'\tau}^{+\infty+i\hat{H}'\tau} dp' e^{-\frac{p'^2}{2}} H_m(p - iH'\tau) \quad (19)$$

Next use $H_m(p - iHt) = \sum_{k=0}^m \binom{m}{k} H_k(p) (-2iH'\tau)^{m-k}$. Note that the contribution from $k = 0$ is just a phase shift of the original projector. In this way we can bound the *additive* error by considering the expansion over $k \geq 1$.

The calculation above shows that detecting a photon number m acts as a symmetrized Hamiltonian polynomial. Complementary to Ref. [34] which investigated *inverse* Hamiltonian polynomials, factors of $(\tau \hat{H}')^m$ can also be investigated as an algorithmic resource, a research direction left for future work. Also note that Eq. (18)'s Hermite basis [35] complements the Chebyshev basis use in quantum signal processing [36].

Alternatively, consider projecting the oscillator to a final CV coherent state $|\beta\rangle = D(\beta)|0\rangle$. A weighted summation of Eq. (18) leads to

$$\hat{P}_{\hat{H}'}(\beta \in \mathbb{C}, \alpha) = \langle \beta|U_{\hat{H}'}^{(B)}(\alpha)|0\rangle_B \quad (20)$$

$$= e^{-i\alpha\beta\hat{H}'} \hat{P}_{\hat{H}'}(\alpha) \quad (21)$$

$$= \sum_n e^{-\frac{(\alpha E_n + i\beta)^2}{2}} |E_n\rangle \langle E_n|. \quad (22)$$

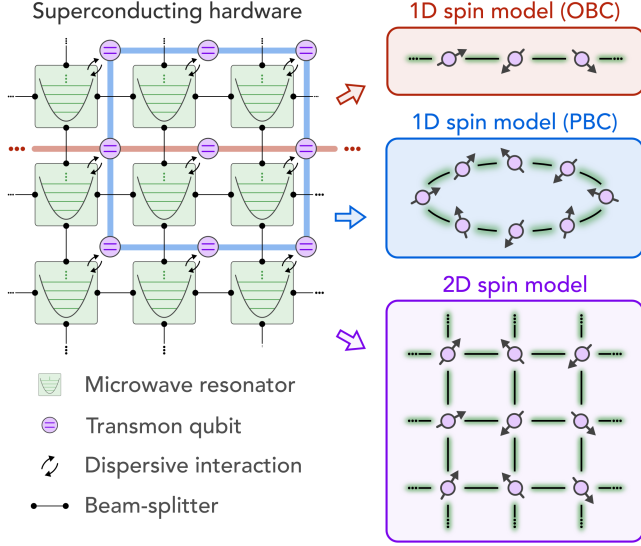


FIG. 2. Hardware layout of 2D superconducting quantum processor (left panel), illustrating the microwave (green) and trasmon qubit (purple) sublattices. The right column indicates embedding 1D geometries with open (OBC) and periodic (PBC) boundary conditions and a 2D generalization. Links between lattice sites are highlighted in green to emphasize that all spin-spin interactions are mediated via the oscillators.

which reduces to Eq. (4) when $\beta = 0$. The above projection onto Gaussian coherent states corresponds to the POVM $\{\frac{1}{\pi}|\beta\rangle\langle\beta|\}$ that can be performed with a heterodyne detector [37–39]. Note the non-orthogonality $\langle\alpha|\beta\rangle \neq \delta_{\alpha,\beta}$ for complex α and β . This POVM satisfies the overcomplete resolution of the identity $\frac{1}{\pi} \int_{\mathbb{C}} d\beta^2 |\beta\rangle\langle\beta| = \mathbb{1}$ where $d\beta^2 = d\Re(\beta)d\Im(\beta)$.

Comparing Eq. (22) with (17), the general $|0\rangle\langle\beta|_B$ block is a potentially powerful oracle, as it not only introduces a global damping factors for all p_n of the mixed state, but also produces a complex shift $i\frac{\beta}{\alpha}$ for each eigenstates. This shift can be interpreted as a real-time evolution $e^{-it\hat{H}'}$ with $t = \alpha\beta$, which commutes with the imaginary-time evolution low-energy filter. Thus, Eqs. (22) and (17) unify (imaginary-time) state preparation and (real-time) dynamical evolution into a single complex-time functional.

Eq. (18) and Eq. (22) both generalize the VTA scattering process and also recovers our initial Gaussian spectral filter Eq. (5), for example through the $m = 0$ measurement. For $m \geq 1$, in the eigenbasis, the wave functions spectral weight is mapped as $|c_\lambda|^2 \rightarrow \frac{(\alpha\hat{H})^{2m}}{m!} e^{-(\alpha\hat{H})^2} |c_\lambda|^2$ which provides a higher energy filter, compared with E_s . Lastly, note that $\text{Tr}_B(|\langle m|U_p(\alpha)|0\rangle|^2) = \sum_{m=0}^{\infty} \hat{P}(m, \tau)^\dagger \hat{P}(m, \tau) = \mathbb{1}_Q$. This means the filters expressed in Eq. (18) are also Kraus operators, with each representing a distinct spectral filter path. Further, they satisfy the necessary completeness relation. One implication is that, by stochasti-

cally tracing over all photon numbers, or phase-space, we recover the logical identity $\mathbb{1}_Q$. This provides a mechanism to construct the identity operator using the oracle-level operations. Later, in Sec. V, we will discuss how this enables protocols which quantify physical error rates.

III. HARDWARE ARCHITECTURE AND COMPILATION

A. Layout and Connectivity

We now compile our eigenvalue transformation oracle with respect to the hardware architecture and ISA detailed in Ref. [15]. As illustrated in Fig. 2, the architectural layout consists of a pair of two-dimensional (2D) sub-lattices resulting in a 2D+1 spatio-temporal architecture. Superconducting transmon qubits (Q) comprise the first sub-lattice. Each qubit is directly coupled to a bosonic (B) harmonic oscillator, which is itself embedded within the second sub-lattice. The 2D qubit coordinates are indexed as $(0, 0) \leq Q := (Q_x, Q_y) \leq (N_x - 1, N_y - 1)$ and, following Eq. (7), appear in the *subscript* of hybrid CV-DV operations. Bosonic qumodes are indices go as $(0, 0) \leq B := (B_x, B_y) \leq (N_x - 1, N_y - 1)$ and appear in the *superscript*. For one-dimensional problems, we omit the y index.

Table I outlines the gates used in our proposed architecture. The DV qubit gates are already well known and do appear below. The CV gates are also well studied and will, for example, involve beam-splitters at the edges connecting the vertices in Fig. 1. The CV-DV gates are discussed in detail below. When oscillator j is dispersively coupled to qubit k , $R_{Z_k}^{(j)}(\theta)$ and $D_{Z_k}^{(j)}(\alpha)$ are *native* hardware operation. If spatially separated, the gate may be accomplished with the overhead of a SWAP network which exchanges the cavity mode from j to the mode physically coupled with qubit k .

B. CV-DV Compilation

Denote the CNOT gate with control on qubit j and target on qubit k gate as CX_{jk} . Two-body phase-rotations can be factorized into the product of a one-body phase rotations and a pair of CNOT gates as

$$R_{Z_j Z_k}(\theta) \equiv e^{-i\frac{\theta}{2} Z_j Z_k} = CX_{jk}^\dagger R_{Z_k}(\theta) CX_{jk}. \quad (23)$$

In this work the qubit-controlled (photon occupation number [15]) parity operator, defined as

$$P_{Z_k}^{(j)} = e^{-i\frac{\pi}{2} Z_k \otimes \hat{a}_j^\dagger \hat{a}_j} = e^{-i\frac{\pi}{2} Z_k \otimes \hat{n}_j}, \quad (24)$$

will be analogous to the CNOT in how it compiles oscillator-controlled two-body interactions. The photon number operator is $\hat{n}_j = \hat{a}_j^\dagger \hat{a}_j = \hat{x}_j^2 + \hat{p}_j^2 - \frac{1}{2}$, so the

Qumode (CV) gates	
$R^{(j)}(\theta)$	$\exp(-i\theta\hat{a}_j^\dagger\hat{a}_j) = \exp(-i\theta\hat{n}_j)$
$F^{(j)}$	$R^{(j)}(\pi/2)$
$D^{(j)}(\alpha)$	$\exp(\alpha\hat{a}_j^\dagger - \alpha^*\hat{a}_j) \equiv \exp(\tilde{\alpha}_j)$
$\text{BS}^{(j,k)}(\theta, \varphi)$	$\exp\left[-i\frac{\theta}{2}\left(e^{i\varphi}\hat{a}_j^\dagger\hat{a}_k + e^{-i\varphi}\hat{a}_j\hat{a}_k^\dagger\right)\right]$
Qubit (DV) gates	
$R_{\vec{m}_j}(\theta)$	$\exp(-i\frac{\theta}{2}\vec{m} \cdot \vec{\sigma}_j)$
Hybrid (CV-DV) gates	
$R_{Z_k}^{(j)}(\theta)$	$\exp(-i\theta Z_k \otimes \hat{n}_j)$
$P_{Z_k}^{(j)}$	$R_{Z_k}^{(j)}(\pi/2)$
$D_{Z_k}^{(j)}(\alpha)$	$\exp\left[Z_k \otimes (\alpha\hat{a}_j^\dagger - \alpha^*\hat{a}_j)\right] = e^{Z_k \otimes \tilde{\alpha}_j}$

TABLE I. Native CV-DV gate set corresponding to the ‘Phase-Space ISA’ in Ref. [15]. Note that $\vec{\sigma}_j = (X_j, Y_j, Z_j)$ is the Pauli operator basis for a spin oriented along an arbitrary axis $\hat{m}_j = (m_x, m_y, m_z)$ on the j th Bloch sphere. The hybrid CV-DV gates are natively available for the case $j = k$. For $j \neq k$, the state of cavity j must be swapped into cavity k to perform the gate controlled by qubit k , and then swapped back to cavity j (see Eq. (30)).

bosonic part of Eq. (24) is generated by the standard quantum Harmonic oscillator interactions, including displacement. Note that $P_{Z_k}^{(j)} = R_{Z_k}^{(j)}(\pi/2)$. Under the qubit-controlled rotation, $R_{Z_k}^{(j)}(t) = \exp(-itZ_k \otimes \hat{n}_j)$, the Heisenberg-picture (i.e., time-shifted) operators are:

$$\begin{aligned} \mathbb{1}_k \otimes \hat{a}_j(t) &\equiv R_{Z_k}^{(j)\dagger}(t) \mathbb{1}_k \otimes \hat{a}_j R_{Z_k}^{(j)}(t) \\ &= e^{-itZ_k} \otimes \hat{a}_j, \end{aligned} \quad (25a)$$

$$\mathbb{1}_k \otimes \hat{x}_j(t) = \cos(t) \mathbb{1}_k \otimes \hat{x}_j + \sin(t) Z_k \otimes \hat{p}_j, \quad (25b)$$

$$\mathbb{1}_k \otimes \hat{p}_j(t) = \cos(t) \mathbb{1}_k \otimes \hat{p}_j - \sin(t) Z_k \otimes \hat{x}_j. \quad (25c)$$

From now on we will omit “ $\mathbb{1}_k \otimes$ ” when there is no confusion. As a special case of the equations above, conjugation by a controlled-parity operator then adjoins a qubit’s $Z_k = \pm 1$ operator to the photon destruction operator

$$P_{Z_k}^{(j)\dagger} \hat{a}_j P_{Z_k}^{(j)} = -iZ_k \otimes \hat{a}_j, \quad (26a)$$

while such conjugation performs Fourier transform on quadrature operators in addition to the Z_k factor

$$P_{Z_k}^{(j)\dagger} \hat{x}_j P_{Z_k}^{(j)} = Z_k \otimes \hat{p}_j, \quad (26b)$$

$$P_{Z_k}^{(j)\dagger} \hat{p}_j P_{Z_k}^{(j)} = -Z_k \otimes \hat{x}_j, \quad (26c)$$

as if the phase space is rotated by $\frac{\pi}{2}$ counterclockwise. Finally we can see that, in direct analogy with Eq. (23), the $P_{Z_k}^{(j)}$ gate maps single-qubit controlled displacements to two-qubit (Ising-interaction) controlled displacements:

$$D_{Z_j Z_k}^{(n)}(\alpha) = e^{-2i\alpha Z_j Z_k \otimes \hat{p}_n} = P_{Z_j}^{(n)\dagger} D_{Z_k}^{(n)}(\alpha) P_{Z_j}^{(n)}. \quad (27)$$

The $P_{Z_j}^{(n)}$ gate also enables us to compile single-qubit controlled displacements (not a native primitive in Fock space ISA) with uncontrolled displacements conjugated by the $P_{Z_k}^{(j)}$ (Fock space ISA) [15]. Local qubit rotations then complete the Heisenberg-interaction gate-set (see Fig. 4 and Sec. IV B for details). As illustrated in Fig. 6, We may then stroboscopically apply such gates to Trotter-approximate real-time evolution. Note that such a cavity-mediated-interaction compilation strategy removes the need for two-qubit entangling gates.

It will also be useful to exchange the qumodes within the B sub-lattice. To do so, we employ the native beam-splitter gate acting on neighboring oscillators j and k

$$\text{BS}^{(j,k)}(\theta, \varphi) = e^{-i\frac{\theta}{2}[e^{i\varphi}\hat{a}_j^\dagger\hat{a}_k + e^{-i\varphi}\hat{a}_j\hat{a}_k^\dagger]}. \quad (28)$$

This couples cavity modes and defines the bosonic (canonical commutation preserving) $\text{SWAP}^{(j,k)} := \text{BS}^{(j,k)}(\pi, 0) F^{(j,k)}$ [40], where the inverse Fourier transform gate (Sec. III.B.2 in Ref. [15]) is $F^{(j,k)} = \exp[i\frac{\pi}{2}(\hat{n}_j + \hat{n}_k)] = F^{(j)} F^{(k)}$. Explicitly,

$$\begin{aligned} &\text{SWAP}^{(j,k)\dagger} \hat{a}_j \text{SWAP}^{(j,k)} \\ &= F^{(j,k)\dagger} \text{BS}^{(j,k)\dagger}(\pi, 0) \hat{a}_j \text{BS}^{(j,k)}(\pi, 0) F^{(j,k)} \\ &= F^{(j,k)\dagger} (-i\hat{a}_k) F^{(j,k)} \\ &= F^{(k)\dagger} F^{(j)\dagger} (-i\hat{a}_k) F^{(j)} F^{(k)} \\ &= F^{(k)\dagger} (-i\hat{a}_k) F^{(k)} = \hat{a}_k. \end{aligned} \quad (29)$$

We now see that $\text{SWAP}^{(k,j)}$ enables us to convert a non-native CV-DV gate $D_{Z_k}^{(j)}(\alpha)$ for $j \neq k$ in Table I into a sequence of native gates as

$$\text{SWAP}^{(j,k)\dagger} D_{Z_k}^{(j)}(\alpha) \text{SWAP}^{(j,k)} = D_{Z_k}^{(k)}(\alpha). \quad (30)$$

In Sec. IV C 1 the SWAP gate is used to couple a single qumode to the entire spin lattice. Afterwards, using M qumodes in Sec. IV D, we will parallelize the QITE filter.

IV. HEISENBERG MODEL COMPILATION

A. Synthesizing Time-Evolution

With Sec. III B describing the required gate set, we proceed to constructively synthesize ε -approximations to the spectral filter \hat{P}_τ . One possible explicit construction of Eq. (14) could be based on Lie-Trotter product formulas (LTPFs). Such LTPFs, based on convergence with re-

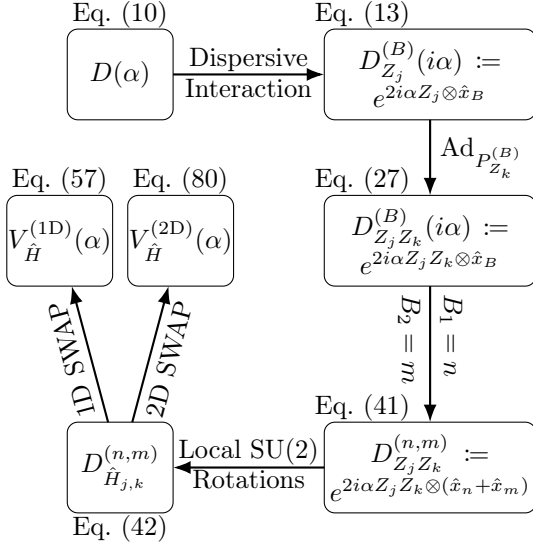


FIG. 3. Compilation workflow where each object represents a relevant quantum operation. The arrows transform the operations, corresponding to the labeled equations, in the Heisenberg picture.

spect to the Euler-Trotter identity $\lim_{r \rightarrow \infty} (e^{A/r} e^{B/r})^r = e^{A+B}$, are useful to approximate exponential functions which are difficult to analytically express due to the exponential's non-commuting generators [41, 42]. Our goal is to now systematically ε -approximate Eq. (5)'s ideal eigenvalue transformation oracle with a block-encoded LTPF $\hat{R}_{\hat{H}'}(\tau)$.

Theorem 3 (Trotter-Hubbard-Stratonovich Formula). *Using $U_{\hat{H}'}^{(p)}(\tau)$ as in Eq. (14), and $V_{\hat{H}'}^{(p)}(\tau)$ as an ε -approximate LTPF suffices to ε -approximate $\hat{P}_{\hat{H}'}(\tau)$ in Eq. (5) with $\hat{R}_{\hat{H}'}(\tau)$ as*

$$\left\| \hat{R}_{\hat{H}'}(\tau) - \hat{P}_{\hat{H}'}(\tau) \right\| = \left\| \langle 0 | V_{\hat{H}'}^{(p)}(\tau) - U_{\hat{H}'}^{(p)}(\tau) | 0 \rangle \right\| \leq \varepsilon. \quad (31)$$

To begin the proof, consider arbitrary 2-local Hamiltonian interaction graph with partitions $\Gamma = \chi'(G)$, where $\chi'(G)$ is the chromatic index of the simple graph $G = (V, E)$ with the vertices V being the lattice sites and the edges E the spin-spin (magnetic exchange) couplings. Using χ' partitions is necessary to ensure that for any γ , all weight-2 Pauli strings in \hat{H}_γ mutually commute. Since $\Delta(G) \leq \chi'(G) \leq \Delta(G) + 1$ (Vizing's theorem), where $\Delta(G)$ is the maximum degree of G (largest coordination numbers for all lattice sites), $\Gamma = \chi'(G) = \mathcal{O}(d)$ for physics relevant lattices in d dimensions, instead of scaling with system size.

Writing the mutually commuting Hamiltonian partitions as $\hat{H} = \sum_{\gamma=1}^{\Gamma} \hat{h}_\gamma$, we use $U_{\hat{H}}^{(\hat{p})}(\alpha) = \lim_{r \rightarrow \infty} [\prod_{\gamma} D_{\hat{h}_\gamma}^{(j)}(\alpha/r)]^r \equiv \lim_{r \rightarrow \infty} V_{\hat{H}}^{\hat{p}}$ as the first-order limiting formula before taking r finite. Recall the vac-

uum wavefunction in momentum basis is $\psi_0(p) = \langle p | 0 \rangle = (2/\pi)^{1/4} e^{-p^2}$, we can then bound the Trotter error as

$$\varepsilon = \left\| \langle 0 | \prod_{\gamma=1}^{\Gamma} e^{-2i\alpha p \hat{h}_\gamma} | 0 \rangle - \langle 0 | e^{-2i\alpha p \sum_{\gamma=1}^{\Gamma} \hat{h}_\gamma} | 0 \rangle \right\| \quad (32)$$

$$= \left\| \int_{-\infty}^{+\infty} dp |\psi_0(p)|^2 \left(\prod_{\gamma=1}^{\Gamma} e^{-2i\alpha p \hat{h}_\gamma} - e^{-2i\alpha p \sum_{\gamma=1}^{\Gamma} \hat{h}_\gamma} \right) \right\|$$

$$\leq \sqrt{\frac{2}{\pi}} \int_{-\infty}^{+\infty} dp e^{-2p^2} \left\| \prod_{\gamma=1}^{\Gamma} e^{-2i\alpha p \hat{h}_\gamma} - e^{-2i\alpha p \sum_{\gamma=1}^{\Gamma} \hat{h}_\gamma} \right\|$$

$$\leq \sqrt{\frac{2}{\pi}} \int_{-\infty}^{+\infty} dp e^{-2p^2} \frac{(2\alpha p)^2}{2} \left\| \sum_{\gamma=1}^{\Gamma-1} \sum_{\delta=\gamma+1}^{\Gamma} [\hat{h}_\delta, \hat{h}_\gamma] \right\| \quad (33)$$

$$= \frac{\alpha^2}{2} \left\| \sum_{\gamma=1}^{\Gamma-1} \sum_{\delta=\gamma+1}^{\Gamma} [\hat{h}_\delta, \hat{h}_\gamma] \right\|. \quad (34)$$

where Eq. (33) used Proposition 9 from Ref. [41].

We will now discuss the circuitry required to conditionally displace an oscillator mode by the energy eigenvalues of a single Hamiltonian interaction between a pair of sites. Note that this Hamiltonian, and commutators between such Hamiltonians, preserve Eq. (35)'s symmetries. We will then provide minimal $\Gamma = 2$ and $\Gamma = 4$ examples in 1D and 2D respectively. To go beyond Theorem 3's analytic result, we also examine a non-color-ordered Trotter sequence which we then numerically simulate.

B. 2-Local Gadget

Consider the Heisenberg model Hamiltonian

$$\hat{H} = \sum_{\langle j,k \rangle} \hat{H}_{j,k} \equiv \sum_{\langle j,k \rangle} J_x X_j X_k + J_y Y_j Y_k + J_z Z_j Z_k, \quad (35)$$

where $\langle j, k \rangle$ indicates nearest-neighbor couplings on a lattice (i.e., a grid graph; for general graph, $\langle j, k \rangle$ denotes the set of edges). Without loss of generality, we target the XXZ spin model Hamiltonian by choosing $J_x = J_y = 1$ and $J_z = \Delta J_x = \Delta$.

Using the native gates in Table I and compilation primitives in Section III B, we compile a displacement gate on qumode n , controlled by the energy of a single bond $\hat{H}_{j,k} = X_j X_k + Y_j Y_k + \Delta Z_j Z_k$, as

$$D_{\hat{H}_{j,k}}^{(n)}(\alpha) = D_{X_j X_k}^{(n)}(\alpha) D_{Y_j Y_k}^{(n)}(\alpha) D_{Z_j Z_k}^{(n)}(\Delta \alpha). \quad (36)$$

This equality leverages the $\mathfrak{su}(4)$ Cartan sub-algebra's ($\{X_j X_k, Y_j Y_k, Z_j Z_k\}$) pairwise commutativity. The first gate required to synthesize Eq. (36) is the conditional displacement controlled by the joint parity $Z_j Z_k$ given in Eq. (27). Using transversal local qubit rotations $V = e^{i\frac{\pi}{4} Y_j} e^{i\frac{\pi}{4} Y_k}$ and $W = e^{-i\frac{\pi}{4} X_j} e^{-i\frac{\pi}{4} X_k}$, we compile

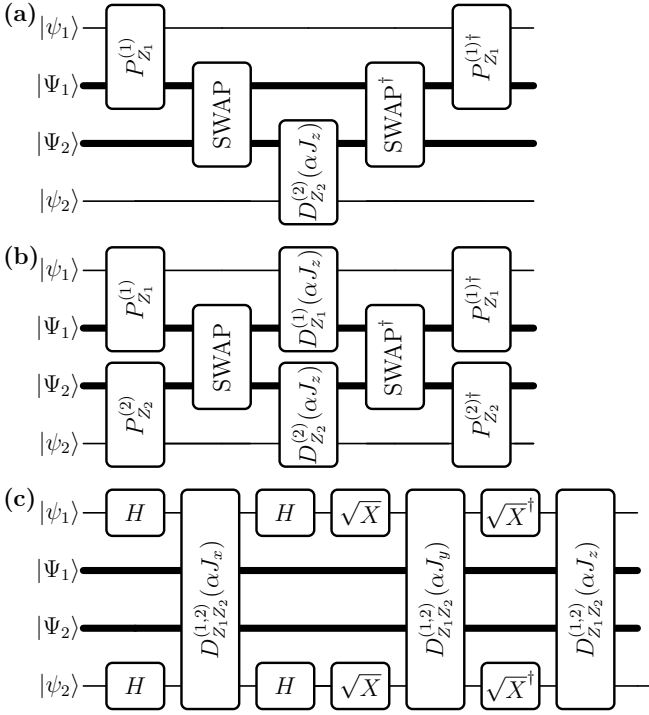


FIG. 4. Compiled circuits for (a) $D_{Z_1 Z_2}^{(1)}$, (b) $D_{Z_1 Z_2}^{(1,2)}$, and (c) $D_{\hat{H}_{1,2}}^{(1,2)} = D_{Z_1 Z_2}^{(1,2)} D_{Y_1 Y_2}^{(1,2)} D_{X_1 X_2}^{(1,2)}$, where $\hat{H}_{1,2}$ is defined in Eq. (36). Thicker wires denote two oscillators (need not be adjacent) in the respective quantum state $|\Psi_1\rangle$ and $|\Psi_2\rangle$; $|\psi_1\rangle$ and $|\psi_2\rangle$ denote the respective states of two qubits linked to their corresponding oscillator.

displacements weighted by the Heisenberg model's off-diagonal interactions

$$D_{X_j X_k}^{(n)}(\alpha) = V^\dagger D_{Z_j Z_k}^{(n)}(\alpha) V, \quad (37)$$

$$D_{Y_j Y_k}^{(n)}(\alpha) = W^\dagger D_{Z_j Z_k}^{(n)}(\alpha) W. \quad (38)$$

Together with Eq. (27), these gates enable the implementation of one round of Eq. (36)'s Heisenberg real-time-evolution operator in a three-stroke clock cycle which will be employed as a building block to synthesize controlled approximations to Eq. (35)'s global energy filter.

C. Parallelizing Compilation in 1D

Our Hamiltonian is a sum of two-local interactions

$$\hat{H} = \sum_{j=0}^{N'} \hat{H}_{j,j+1}. \quad (39)$$

For open boundary conditions (OBC), $N' = N - 2$, while for periodic boundary conditions (PBC), $N' = N - 1$ with $N' + 1 \equiv 0$ (i.e., indices are modulo N). Now consider an additive factorization of Eq. (39) into the two terms cor-

responding interactions on even (\hat{A}) and odd (\hat{B}) edges, $\hat{H} = \hat{A} + \hat{B}$. Without loss of generality we take N even, such that

$$\hat{A} = \sum_{j=0}^{\frac{N}{2}-1} \hat{H}_{2j,2j+1} \equiv \sum_j \hat{A}_j, \quad (40a)$$

$$\hat{B} = \sum_{j=0}^{\frac{N}{2}-1} \hat{H}_{2j+1,2j+2} \equiv \sum_j \hat{B}_j. \quad (40b)$$

The 2-coordinated nearest-neighbor Hamiltonian interaction can be additively factorized, in that each equation in Eq. (40) is a sum over terms with *disjoint* support which was not the case in Eq. (39). This proves that $[\hat{A}_j, \hat{A}_k] = [\hat{B}_j, \hat{B}_k] = 0$, a fact that will be used to parallelize a controlled operation over the global operator \hat{A} or \hat{B} . Recalling that $\hat{H}_{j,j+1} = X_j X_{j+1} + Y_j Y_{j+1} + \Delta Z_j Z_{j+1}$ was compiled in Sec. IV B, our task is now to (i) explain how a single oscillator may play the role of the block encoding ancilla qumode and (ii) explain how this sequence can be embarrassingly parallelized using a lattice of qumodes. We now examine (i), before outlining (ii) in 1 and 2 dimensions.

1. One-Oscillator Compilation

Before proceeding to the fully parallelized compilation let us first compile dynamics of Eq. (35) controlled on a single ($M = 1$) qumode. Following the color ordering presented above, we displace the oscillator by \hat{A} and then subsequently by \hat{B} . This is achieved by serially displacing by each bond in \hat{A} . To do so, a pair of SWAPs will route the bosonic mode around the spin chain, displacing by each term in \hat{A} along the way. Repeating for each of the terms in \hat{B} then realizes a first order LTPF $e^{\hat{B}} e^{\hat{A}}$ of Eq. (35). Using N SWAPs to evolve by each colored partition, the resulting Trotter formula $V_{\hat{H}}(\alpha) = e^{-i2\alpha\hat{p}\hat{B}} e^{-i2\alpha\hat{p}\hat{A}}$ is related to our target dynamics through $V_{\hat{H}}(\alpha) = U_{\hat{H}}^{(p)}(\alpha) + \mathcal{A}(\alpha)$ where the additive error is bounded in Theorem 3.

2. Two-Oscillator Compilation

The next step in our progression is to parallelize the compilation sequences of adjacent oscillators. We will return to formally generalize this result in Sec. IV E. The second oscillator, indexed as k , can also be displaced conditional on the commuting disjoint components of \hat{A} (and subsequently \hat{B}) in parallel with the first oscillator.

Note that an Ising interaction can, since $[D_{Z_j Z_k}^{(j)}(\alpha), D_{Z_j Z_k}^{(k)}(\alpha)] = 0$, control the displacements the involved oscillators in any order. Since the Ising generators commute, both adjacent oscillators can then

be simultaneously displaced using the $P_{Z_k}^{(j)}$ and $P_{Z_j}^{(k)}$ gates as illustrated in Fig. 3 which results in

$$\begin{aligned} D_{Z_j Z_k}^{(j,k)}(\alpha) &= D_{Z_j Z_k}^{(j)}(\alpha) \times D_{Z_j Z_k}^{(k)}(\alpha) \\ &= e^{-2i\alpha Z_j Z_k \otimes (\hat{p}_j + \hat{p}_k)}. \end{aligned} \quad (41)$$

The same is true when compiling the two-qumode displacement conditioned on a single bond's Heisenberg-interaction spectra as

$$\begin{aligned} D_{\hat{H}_{jk}}^{(n,m)}(\alpha) &= D_{X_j X_k}^{(n,m)}(\alpha) \times D_{Y_j Y_k}^{(n,m)}(\alpha) \times D_{Z_j Z_k}^{(n,m)}(\Delta\alpha) \\ &= e^{-2i\alpha(X_j X_k + Y_j Y_k + \Delta Z_j Z_k) \otimes (\hat{p}_n + \hat{p}_m)} \\ &= e^{-2i\alpha \hat{H}_{jk} \otimes (\hat{p}_n + \hat{p}_m)}. \end{aligned} \quad (42)$$

In addition to a color-ordered-decomposition which is helpful in simplifying the proof of Theorem 3, to minimize entangling gate-count pre-factors it will also be useful to consider controlled displacements made up of terms such as $D_{\hat{B}_j}^{(j+1)}(\alpha) D_{\hat{A}_j}^{(j)}(\alpha)$. Here, conditioned on different colored interactions within the same time step, adjacent oscillators are displaced. In this case, for each oscillator, N SWAPS be used in order to conditionally displace the each of the modes on the individual terms comprising \hat{A} and \hat{B} in an alternating series. That is, each oscillator sweeps around the spin chain and is displaced by each bond in serial. This is in contrast to the color-ordering above where the number of SWAPS acting on each mode is double the length of the chain. To get a picture for how the two Trotter orderings compare, see Fig. 7 and Fig. 10 where panels (a) and (b) correspond to the color-ordered and \hat{A} - \hat{B} alternating ordered Trotterizations respectively. In Sec. IV D we will concretely specify how SWAP operations enable a parallelized, multi-oscillator compilation.

D. Multi-Oscillator Compilation

In Fig. 1 qumode resources scale extensively with the principal system's size. We may therefore reduce the overall time by parallelizing the total displacement into the product of many shorter displacements.

For the hardware where each qubit is directly controlled by an associated oscillator, i.e., with $M = N$ oscillators, we fully parallelize the energy filter over the many oscillator modes. To do so we must synthesize a ε -approximation where *all* oscillators are displaced by \hat{H} . Since our filter is a quadratic function of $\hat{H}'\alpha$, $\hat{P}_{\hat{H}'}(\alpha)^{\frac{1}{M}} = \hat{P}_{\hat{H}'}(\alpha/\sqrt{M})$. Thus, assigning the re-scaled time α/\sqrt{M} to each of the M distinct spatial oscillators, one may parallelize $\tau = \alpha$ in the imaginary time evolution operator in Theorem 3 (Trotter-Hubbard-Stratonovich Formula).

Since the native gate time depends on the magnitude of the displacement, displacing individual oscillators by α/\sqrt{M} reduces the physical execution time

of our algorithm while maintaining the same scaling of Trotter error as in the single oscillator case. Note that the first-order Trotter error per oscillator becomes $\mathcal{O}(N(\alpha/\sqrt{M})^2)$, but the total Trotter error of M -factors scales as $M \cdot \mathcal{O}(N(\alpha/\sqrt{M})^2) = \mathcal{O}(N\alpha^2)$, the same as the single oscillator case. As a result, we now see how parallelizing over hardware-native oscillators reduces the absolute algorithmic runtime by a factor \sqrt{M} . Generalizing a single oscillator variable \hat{p}_0 block-encoding, to an M oscillator $\{\hat{p}_j\}_{j=0}^{M-1}$ block encoding, we have:

Lemma 4 (Spacetime Parallelization).

$$\begin{aligned} \hat{P}_{\hat{H}'}(\alpha) &= \langle 0 | U_{\hat{H}'}^{(p_0)}(\alpha) | 0 \rangle \\ &= \langle 0 | \prod_{j=0}^{M-1} U_{\hat{H}'}^{(p_j)}\left(\alpha/\sqrt{M}\right) | 0 \rangle \quad (43) \\ &= \bigotimes_{j=0}^{M-1} \langle 0_j | U_{\hat{H}'}^{(p_j)}\left(\alpha/\sqrt{M}\right) | 0_j \rangle \quad (44) \end{aligned}$$

In the top line, one oscillator and \sqrt{M} serial time resources are utilized. The second line uses M oscillators as spatial resources to control spin dynamics and requires an M -fold tensor product measurement to generalize Eq. (31) to the multi-oscillator limit. Upon measuring the vacuum configuration $|0\rangle = |0\rangle^{\otimes M}$, after the application of $\prod_{j=0}^{M-1} U_{\hat{H}'}^{(p_j)}\left(\alpha/\sqrt{M}\right)$, we have Eq. (4).

The last step to complete end-to-end compilation is the synthesis of a ε -approximate of Lemma 4. While block-encoded ε -approximations of unitaries offer scaling advantages, keeping near-term applications in mind, we synthesize a Trotter approximation.

Theorem 5 (Parallelized LTHS Formula). *Consider a general 2-local spin (spectrum-shifted) Hamiltonian $\hat{H} = \sum_{\gamma=1}^{\Gamma} \hat{H}_{\gamma}$ partitioned into Γ parts $\{\hat{H}_{\gamma} \mid \hat{H}_1 = \hat{A}, \hat{H}_2 = \hat{B}, \hat{H}_3 = \hat{C}, \dots\}$ according to a proper edge coloring of the interaction graph of \hat{H} so that all weight-2 Pauli strings mutually commute in each \hat{H}_{γ} . There exists a coloring so that $\Gamma - 1$ is less than or equal to the largest coordination number of any site in the system (Vizing's theorem), and thus the number of partitions is bounded by the system size. With controlled displacement $U_{\hat{H}}^{(p_j)}(\tau = \alpha/\sqrt{M})$ as in Eq. (14) for M oscillators respectively in parallel, an exact ground state projection (GSP) operator is given by the vacuum transition probability (VTA)*

$$\hat{P}_{\hat{H}}(\alpha) = \langle 0 | \prod_{j=0}^{M-1} U_{\hat{H}}^{(p_j)}\left(\frac{\alpha}{\sqrt{M}}\right) | 0 \rangle = e^{-\alpha^2 \hat{H}^2/2}. \quad (45)$$

The LTHS synthesized approximation is given by

$$\hat{R}_{\hat{H}}(\alpha) = \langle 0 | \prod_{\gamma=1}^{\Gamma} \left[\prod_{j=0}^{M-1} U_{\hat{H}_{\gamma}}^{(p_j)}\left(\frac{\alpha}{\sqrt{M}}\right) \right] | 0 \rangle \quad (46a)$$

$$= \mathcal{T}_\gamma e^{-\alpha^2 (\sum_\gamma \hat{H}_\gamma)^2 / 2}, \quad (46b)$$

where the γ (color) ordering \mathcal{T}_γ is analogous to Feynman's time order operator. The Lie-Trotter series' commutator-scaling additive error is

$$\varepsilon = \left\| \hat{R}_{\hat{H}}(\alpha) - \hat{P}_{\hat{H}}(\alpha) \right\| \leq \frac{\alpha^2}{2} \sum_{\gamma_1 < \gamma_2} \left\| [\hat{H}_{\gamma_1}, \hat{H}_{\gamma_2}] \right\|. \quad (47)$$

If \hat{H} is a Heisenberg spin model, Eq. (46) can be simplified to the following form:

$$\begin{aligned} \hat{R}_{\hat{H}}(\alpha) = & \sum_{\{b_{i,j}\} \in \{0,1\}^{|E|}} e^{-\alpha^2 [E_s + \sum_{(i,j) \in E} (4b_{i,j} - 1)]^2 / 2} \\ & \times \mathcal{T}_\gamma \prod_{(i,j) \in E} \frac{(3 - 2b_{i,j}) + (1 - 2b_{i,j})\hat{H}_{i,j}}{4}, \end{aligned} \quad (48)$$

where the color ordering is trivial for the product of triplet (singlet) projectors $\frac{3 + \hat{H}_{i,j}}{4}$ for $b_{i,j} = 0$ ($\frac{1 - \hat{H}_{i,j}}{4}$ for $b_{i,j} = 1$) over the edge set $E = \{(i,j) \mid \hat{H}_{i,j} = X_i X_j + Y_i Y_j + Z_i Z_j \neq 0\}$ with Heisenberg interactions.

The proof of Eqs. (46) to (48) is given in Appendix B. The analytical expression of $\hat{R}_{\hat{H}}(\alpha)$ in Eq. (48) for 1D chain colored as in Fig. 5(a) is given in Appendix C.

In this scheme the circuit depth scales extensively with the system size, similar to a single oscillator, and $\hat{R}_{\hat{H}}(\alpha)$ compiled by parallelized gate sequences which are copies of the single oscillator circuitry. However, assuming the $D_{\hat{H}}^{(j)}(\tau)$'s gate duration on real hardware is proportional to τ [15], the time complexity is reduced by a factor \sqrt{M} from the single oscillator case.

E. 1D SWAP Networks

We now describe the role SWAP networks (SNs) for qumodes consisting of beam splitters play in parallelized, multi-oscillator compilation. Namely, the SNs spatially cycle all oscillators while synchronizing their controlled-time-evolution gates. As illustrated in Fig. 1 by the two boxes with arrows, each oscillator is displaced conditioned on a two-body interaction localized at an edge connecting two qubits on a graph, and this primitive operation is implemented by the circuit in Fig. 4(c) for Eq. (40).

Now, exploiting Lemma 4's freedom and our hardware's ability to parallelize displacements of nonadjacent oscillators, we use Eq. (42) and Eq. (40) to define two edge-colored displacement operators

$$D_{\hat{A}}(\alpha) = \prod_{j=0}^{\frac{N}{2}-1} D_{A_j}^{(2j, 2j+1)}(\alpha) \quad (49a)$$

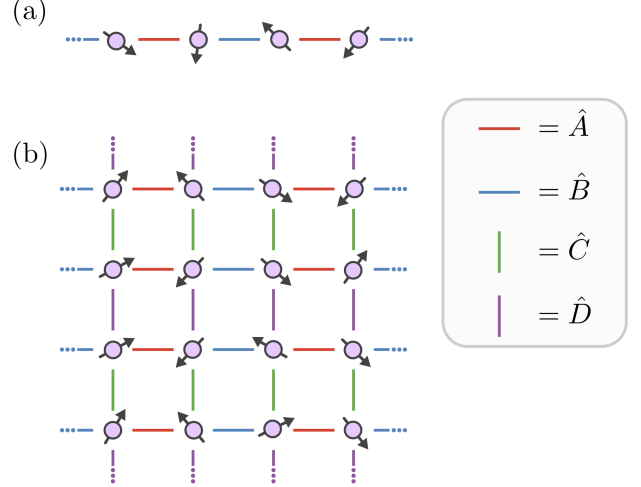


FIG. 5. Trotter orderings for 1D (a) and 2D (b) spin models. Each color denotes spin-spin interaction terms for which conditional oscillator displacements can be parallelized. (a) In 1D, this results in alternating sequence of displacements corresponding to red (\hat{A}) and blue (\hat{B}) links. In 2D, interaction terms are grouped by red (\hat{A}), blue (\hat{B}), green (\hat{C}), and purple (\hat{D}) links.

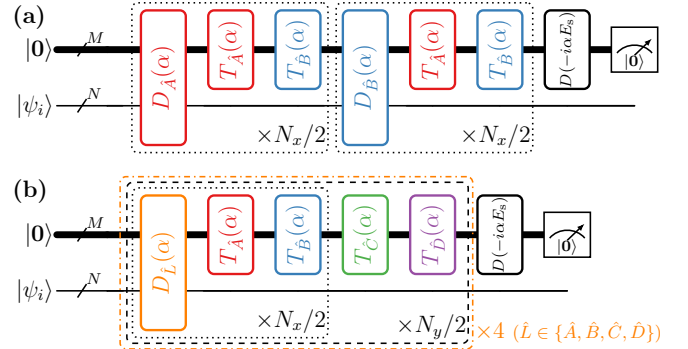


FIG. 6. Quantum realization of the color-ordered Trotter-approximated Hamiltonian displacement in (a) 1D Eq. (57) and (b) 2D Eq. (81). The initial state of the CV-DV system is $|0\rangle \otimes |\psi_i\rangle$ with M qumodes in the all-vacuum state $|0\rangle = |0\rangle^{\otimes M} = |0 \dots 0\rangle$ and N qubits in the state $|\psi_i\rangle$. We assume $M = N$. The slash symbol denotes the bundle of quantum wires (thicker bundled wires for CV system). In (b) \hat{L} is substituted with \hat{A} , \hat{B} , \hat{C} , or \hat{D} for each of the four repetitions of the circuit part enclosed in the dash-dotted orange box.

$$D_{\hat{B}}(\alpha) = \prod_{j=0}^{\frac{N}{2}-1} D_{B_j}^{(2j+1, 2j+2)}(\alpha). \quad (49b)$$

This pair of operators displaces pairs of oscillators by single pieces of the \hat{A} , or \hat{B} , Hamiltonian partition. Therefore, oscillators at even (odd) cavities must be routed to even (odd) cavities if they are to be displaced by the next term of the same colored interaction at the next step. De-

fine the transversal (T) bosonic SWAP operators as

$$T_{\hat{A}} = \bigotimes_{j=0}^{\frac{N}{2}-1} \text{SWAP}^{(2j, 2j+1)}, \quad (50a)$$

$$T_{\hat{B}} = \bigotimes_{j=0}^{\frac{N}{2}-1} \text{SWAP}^{(2j+1, 2j+2)}. \quad (50b)$$

Acting along the bonds illustrated in Fig. 5, these gates permute bosonic modes on all bonds of a given color. The global effect is to exchange all modes along one color's edges, equivalent to a total translation of one lattice constant for A -sublattice and B -sublattice respectively in the opposite direction. Since $T_{\hat{A}}^2 = T_{\hat{B}}^2 = \mathbb{1}$, we instead define the back-to-back execution of Eqs. (50a) and (50b) as the composite permutation

$$T_{\hat{A}\hat{B}} = T_{\hat{B}} T_{\hat{A}}. \quad (51)$$

$T_{\hat{A}\hat{B}}$ translates the oscillators by two lattice sites for A/B -sublattices in the opposite directions as

$$T_{\hat{A}\hat{B}}(\hat{a}_j) \equiv T_{\hat{A}\hat{B}}^\dagger \hat{a}_j T_{\hat{A}\hat{B}} = \begin{cases} \hat{a}_{j+2} & \text{if } j \text{ is even,} \\ \hat{a}_{j-2} & \text{if } j \text{ is odd.} \end{cases} \quad (52)$$

such that p iterations of $T_{\hat{A}\hat{B}}$ shifts by $2p$ sites.

$$T_{\hat{A}\hat{B}}^p(\hat{a}_j) = \begin{cases} \hat{a}_{j+2p} & \text{if } j \text{ is even,} \\ \hat{a}_{j-2p} & \text{if } j \text{ is odd.} \end{cases} \quad (53)$$

Assuming even N , we see that $T_{\hat{A}\hat{B}}^{\frac{N}{2}} = \mathbb{1}$, which implies that $\frac{N}{2}$ applications return each mode to its original cavity

$$T_{\hat{A}\hat{B}}^{\frac{N}{2}}(\hat{a}_j) = \hat{a}_j. \quad (54)$$

Naturally, these relations lead us to assign a group structure for these permutations. We define an element of the symmetric group $\tau \in S_N$ which, after p iterations of $T_{\hat{A}\hat{B}}$, maps oscillator indices to cavity indices as

$$\tau^p(j) = \begin{cases} j + 2p \pmod{N} & \text{if } j \text{ is even,} \\ j - 2p \pmod{N} & \text{if } j \text{ is odd.} \end{cases} \quad (55)$$

By interspersing the translation operators with Eq. (49) we are able to use *each* oscillator to control each color partition's time-evolution. Leveraging this, the two steps comprising the 1D Trotter-factorized approximation are:

$$(T_{\hat{A}\hat{B}} D_{\hat{B}}(\alpha))^{\frac{N}{2}}$$

$$= \prod_{p=0}^{\frac{N}{2}-1} \exp \left\{ -2i\alpha \sum_j B_j \otimes (\hat{p}_{\tau^p(j)} + \hat{p}_{\tau^p(j+1)}) \right\}, \quad (56a)$$

$$(T_{\hat{A}\hat{B}} D_{\hat{A}}(\alpha))^{\frac{N}{2}} \\ = \prod_{q=0}^{\frac{N}{2}-1} \exp \left\{ -2i\alpha \sum_j A_j \otimes (\hat{p}_{\tau^q(j)} + \hat{p}_{\tau^q(j+1)}) \right\}. \quad (56b)$$

Together these two operators are composed to construct the Trotterized global Hamiltonian displacement. This provides an end-to-end compilation of the expressions in Theorem 3 and Theorem 5. In Fig. 6 we present a quantum circuit realizing

$$(T_{\hat{A}\hat{B}} D_{\hat{B}}(\alpha))^{\frac{N}{2}} \times (T_{\hat{A}\hat{B}} D_{\hat{A}}(\alpha))^{\frac{N}{2}} = V_{\hat{H}'}(\alpha). \quad (57)$$

F. Numerical Results

To demonstrate and verify our algorithm, we consider the case of $N = 4$ site antiferromagnetic Heisenberg model and give numerical simulation results below, with some additional analytical results included in Appendix C. In Fig. 7 the two panels present visual representations of the color-ordered (a) and alternating-ordered (b) Trotter scheme compilations. In addition, to help build further intuitive understanding of the use of SNs in each clock cycle, Fig. 10 in Appendix D presents visual representations of the two compilations for a 6-site chain. It is easy to see that, in 1D case with $\Gamma = 2$ colorable chain, the number of SNs (i.e., $T_{\hat{A}\hat{B}}$) is $\Gamma(N_x/2 - 1) = N_x - 2$ for (a)-compilation sequence and $N_x/2 - 1$ for (b)-compilation sequence. Note that (a)-compilation sequence strictly follows Fig. 6(a), except that the final layers of $T_{\hat{A}}$ and $T_{\hat{B}}$ in each dashed box in Fig. 6(a) are dropped without affecting the result since $-2i\alpha \sum_j \hat{p}_j$ is permutation invariant.

1. $\alpha \ll 1$ LTPF Regime

Using $\beta = \alpha(1 - \frac{E_s}{N})$, we approximately displace all oscillators by the spectrum-shifted Hamiltonian \hat{H}' via the first order product formula

$$\prod_{p=0}^{N-1} e^{-2i\alpha \hat{B}' \otimes \hat{p}_p} \times \prod_{q=0}^{N-1} e^{-2i\alpha \hat{A}' \otimes \hat{p}_q} \\ = \exp \left(-2i\alpha \hat{B}' \otimes \sum_j \hat{p}_j \right) \exp \left(-2i\alpha \hat{A}' \otimes \sum_j \hat{p}_j \right). \quad (58)$$

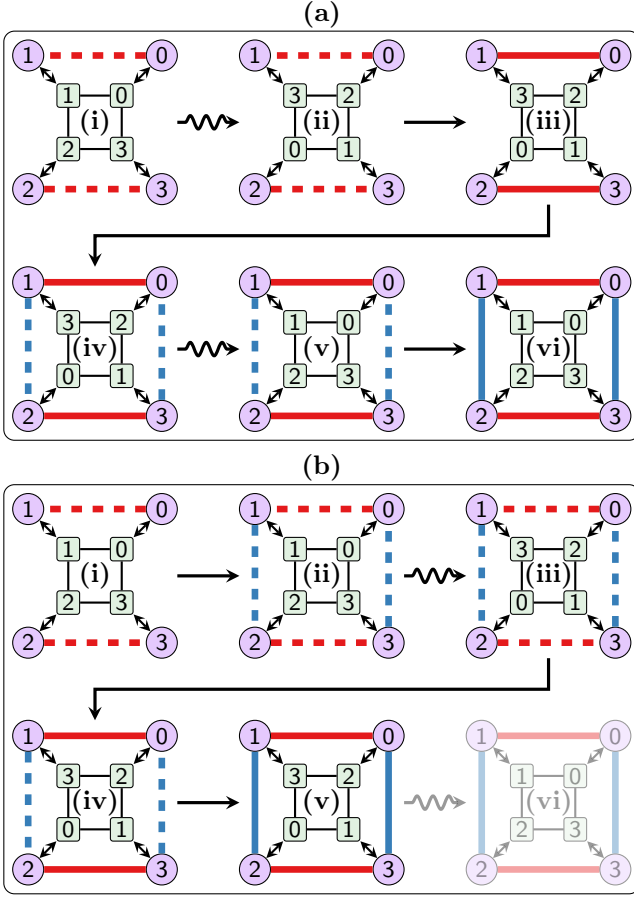


FIG. 7. Visual representations of the compilations for $N = 4$ site Heisenberg model. Purple circular nodes are qubits and light green square nodes are qumodes. The panel (a) strictly follows the sequence of gate operations illustrated in Fig. 6(a), while the panel (b) gives an alternative ordering of the sequence to couple \hat{H}_γ terms of the same color to respective qumodes, resulting in a shortened circuit compared to Fig. 6(a). Wavy-line arrows indicate that only qumode SWAP network operations are applied; straight-line arrows indicate that the circuit in Fig. 4(c) are applied in parallel to all edges of one color [including in step (i)]. For colored edges representing \hat{H}_γ terms, dashed-line means coupling \hat{H}_γ to a half of the qumodes and solid line all qumodes. The final SWAP network is not necessary in panel (b).

Recalling the ground state energy shift, define

$$\hat{A}' = \left(\sum_{j=0}^{\frac{N}{2}-1} \hat{H}_{2j,2j+1} \right) - \frac{E_s}{2} \equiv \sum_j \hat{A}_j - \frac{E_s}{N}, \quad (59a)$$

$$\hat{B}' = \left(\sum_{j=0}^{\frac{N}{2}-1} \hat{H}_{2j+1,2j+2} \right) - \frac{E_s}{2} \equiv \sum_j \hat{B}_j - \frac{E_s}{N}, \quad (59b)$$

such that $\hat{H}' = \hat{A}' + \hat{B}' = \hat{H} - E_s$. In one-dimension we partition the interactions into two sets of generators $\hat{H} = \sum_{j=1}^{j=L} H_{j,j+1} = \hat{A} + \hat{B}$. For such a system, the

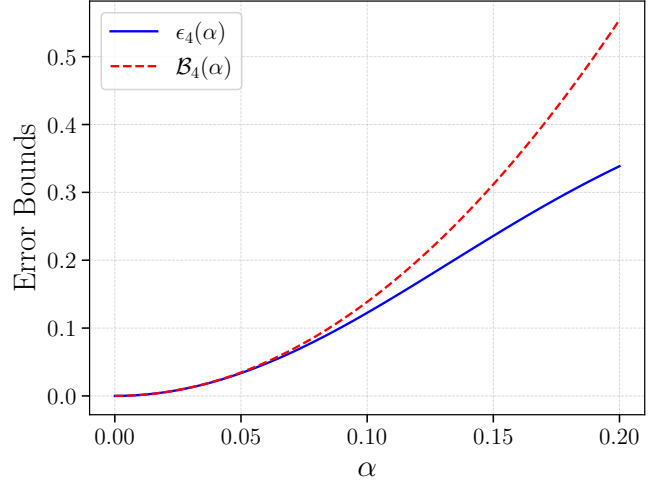


FIG. 8. Comparison of the additive Trotter error $\epsilon_N(\alpha) = \|\hat{R}_{H'}(\alpha) - \hat{P}_{H'}(\alpha)\|$ and the scaling bound $B_N(\alpha) = \frac{\alpha^2}{2} \sum_{\gamma_1 < \gamma_2} \left\| [\hat{H}_{\gamma_1}, \hat{H}_{\gamma_2}] \right\|$ for a target system of $N = 4$ sites with $\Gamma = 2$ partitions. For these simulations we use the spectral norm $\|\hat{M}\|_2 \equiv \sigma_{\max}(\hat{M}) = \sqrt{\lambda_{\max}(\hat{M}^* \hat{M})}$, i.e., the largest singular value of \hat{M} . These results agree with Eq. (47) in Theorem 5 since $\epsilon_N(\alpha) \leq B_N(\alpha) \forall \alpha \geq 0$.

first-order Trotter expansion

$$e^{i\tau\hat{H}} = \left(e^{i\tau\hat{A}/r} \cdot e^{i\tau\hat{B}/r} \right)^r + \mathcal{O}\left(\left\| [\hat{A}, \hat{B}] \right\| \tau^2 / r\right). \quad (60)$$

When $\|[\hat{A}, \hat{B}]\| \tau^2 / r \leq 1$ this expansion is valid, and bound to the ideal dynamics up by the above additive error. Next we apply the interaction for each set controlled on the qumode. The interactions are stroboscopically repeated to realized a bounded Lie-Trotter expansion of the target Hamiltonian's real-time evolution.

Inserting the product formula Eq. (60) into Eq. (8) generates a formula for the error in approximating the target imaginary-time spectral projection given by Eq. (4). The Hubbard-Stratonovich transformation in Eq. (8) synthesizes an imaginary-time evolution as a linear superposition over real-time evolutions. This connection provides a useful tool to analyze imaginary-time propagation errors from the existing theory on Trotter errors established for real-time evolution [41]. For example, for composite Hamiltonian \hat{H}' as a sum of many terms, a p th order Trotterization of $e^{-i\hat{H}'\tau x}$ on the RHS of Eq. (8) for small τ effectively produces a $2p$ th order imaginary-time evolution on the LHS (due to τ^2) via the integral transformation with the weight $e^{-\frac{1}{2}x^2}$.

As we demonstrated in Sec. IV, given qubit-oscillator hardware connectivity, Trotterization suffices to compile the real-time evolution of a Hamiltonian \hat{H}' comprised of non-commuting terms. The HS transform provides a concrete way to analyze the error in our projection

scheme using existing error analysis for real-time evolution. We note that the synthesis of real-time evolution with high-order Trotter errors from a linear combination of low-order product formulas via error cancellation has been explored to construct effective multi-product formulas for efficient Hamiltonian simulation [21, 43–45]. From this perspective, the HS transform, as a linear combination of real-time evolution, is a Gaussian multi-product formula for imaginary-time propagation.

2. $\alpha \gg 1$ Floquet-Regime

In this periodic evolution, an effective Floquet operator emerges. Due to the large displacement in this limit, a perturbative analysis is not useful. Rather, thinking about the underlying symmetries of the evolution and hybridization between sectors gives us an understanding of Floquet processes. Based on the result of combining this limit, with the Lie-Trotter limit, we optimize the displacement factor α in the next section. As we see in Fig. 9 for a 4-site XXZ model ($\Delta = 1$) with a single Trotter step $r = 1$, the total and Trotter spectral modes converge in the $\alpha \gg 1$ limit. The Floquet spectrum converges to a fixed point in the large α limit. The spectra share similar features, partially enforced by the unbroken S^2 and S_{tot}^Z symmetries.

3. Optimization

We now present numerical simulations for the energy filter. To analyze cases which are most amenable to experiments, i.e., which minimize all prefactors in the resource overhead, we analyze a filter realized by the alternating-color controlled displacement Trotterization as illustrated in panel (b) of Fig. 7. Here the number of SNs is half the spatial extent of the system, whereas the number of SNs is directly proportional to the spatial extent of the system in the color ordering. While both display the same asymptotic scaling, removing this extra pre-factor of 2 may prove useful in experimental implementations where physical errors dominate over algorithmic errors. We defer a more detailed discussion of experimental errors to Sec. V.

The rate at which spectral operations, including \hat{R}_α 's ground state projection, transform depends on spectral features. First, the magnitude of the projector's smallest eigenvalue λ_0 , and its proximity to E_s , quantifies the preservation of the ground state ($|\lambda_0\rangle$) after oscillator measurement. Secondly, QITE projection depends on the proximity of eigenvalues. Denote the first-excited synthesized eigenvalue as λ_1 . A large low-energy multiplicative condition number, $\kappa_{0,1} = \lambda_0/\lambda_1$, implies efficient ground state preparation. In terms of the additive spectral gap $\Delta_{0,1} = \lambda_1 - \lambda_0$, has previously been analyzed [19, 20, 22]. This begs the question of whether there exists an optimal α , i.e., one that optimizes state preparation.

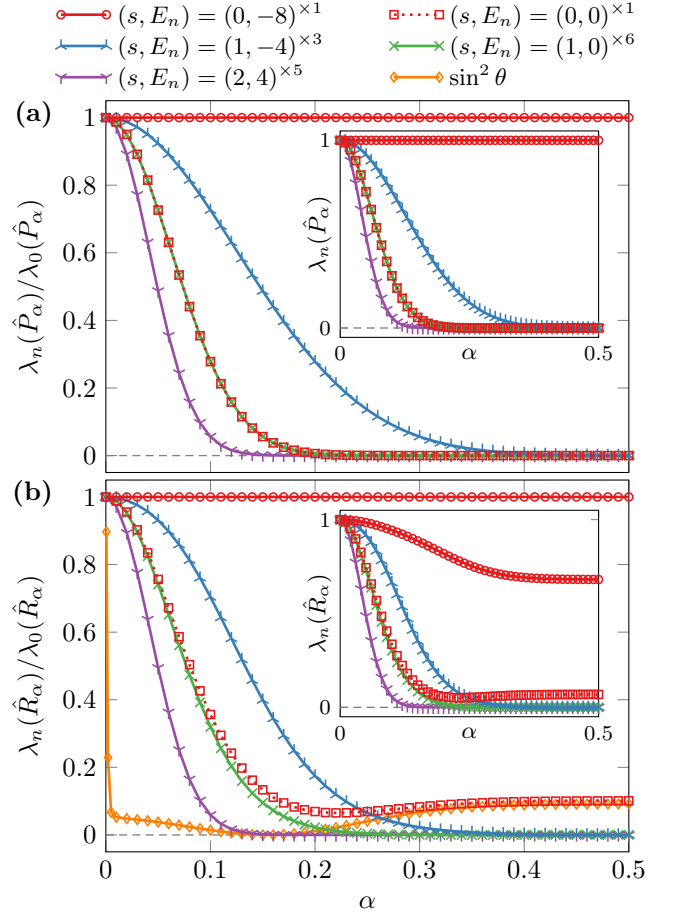


FIG. 9. The normalized eigenvalues of (a) exact projector \hat{P}_α and (b) Trotter-approximate projector \hat{R}_α for $N = 4$ site antiferromagnetic Heisenberg model. The insets show the unnormalized values. Here, $\lambda_n(\hat{O})$ denotes the n th (right-)eigenvalue for the (non-)Hermitian operator ($\hat{O} = \hat{R}_\alpha$) $\hat{O} = \hat{P}_\alpha$. The value of normalization factor $\lambda_0(\hat{O})$ is shown by the red solid curve with circles in the insets. Since \hat{P}_α and \hat{H} share common eigenvectors, $\hat{P}_\alpha = \sum_n \lambda_n(\hat{P}_\alpha) |E_n\rangle\langle E_n|$ and thus eigenvalues of \hat{P}_α are filtering weights of each individual eigenvector projector $|E_n\rangle\langle E_n|$, where $|E_0\rangle$ denotes the ground state of Hamiltonian. In general the ground state projector has larger *relative* weight as α increases and $\lambda_{n \neq 0}$ decreases (except that for the red dotted curves with squares in panel (b), the maximal ratio $\lambda_0(\hat{R}_\alpha)/\lambda_n(\hat{R}_\alpha)$ is at $\alpha \sim 0.2$). The symbols are from numerical simulation and the lines are from analytical expressions. In the legend different curves are labeled by the corresponding conserved quantum number s (total spin) and E_n (energy) and the degeneracy d_g is marked by “ $\times d_g$ ” superscript. However, in (b), the two red curves (circles and squares) of \hat{R}_α have slightly hybridized E_n eigenvectors and the degree of mixtures is shown by the orange curve for $\sin^2 \theta$ (see main text). At $\alpha \sim 0.15$, $\sin^2 \theta = 0$, so the energy is conserved and the α value is optimal for projection.

In our numerical simulations, of the 4-site XXZ model consisting of four qubits and the low-photon number subspace of four qumodes, we now describe convolution of the aforementioned spectral competitions with couplings between states within the projector's spin-0 sector. The detailed analytical results are given in Appendix C. One can analytically show that \hat{R}_α is block-diagonal in the eigenbasis of \hat{H}_4 [46] and can be decomposed as

$$\hat{R}_\alpha = \hat{R}_\alpha^{(0)} \oplus \left(\hat{R}_\alpha^{(1)} \oplus \hat{R}_\alpha^{(2)} \right) \quad (61)$$

where $\hat{R}_\alpha^{(1,2)} = \hat{R}_\alpha^{(1)} \oplus \hat{R}_\alpha^{(2)}$ is a 14-dimensional diagonal matrix containing the spin-1 and spin-2 eigenstates and

$$\hat{R}_\alpha^{(0)} = r_{00} |\lambda_0\rangle\langle\lambda_0| + r_{01} |\lambda_0\rangle\langle\lambda_1| \quad (62)$$

$$+ r_{10} |\lambda_1\rangle\langle\lambda_0| + r_{11} |\lambda_1\rangle\langle\lambda_1| \quad (63)$$

$$= \begin{pmatrix} r_{00} & r_{01} \\ r_{10} & r_{11} \end{pmatrix} \quad (64)$$

is a nondiagonal matrix containing the two spin-0 eigenstates. The off-diagonal entries in $\hat{R}_\alpha^{(0)}$ correspond to the state-transfer terms that mix the ground state $|\lambda_0\rangle$ ($E_s = -8$) and higher-energy state $|\lambda_1\rangle$ ($E_s = 0$) with a coupling strength governed by $r_{01} = -r_{10}$.

If $|r_{01}|$ were minimized at some α_{optimal} , then \hat{R}_α would be approximately, if not actually, diagonal, and hence an ideal projector. As shown in Fig. 9, we successfully decouple $|\lambda_0\rangle$ and $|\lambda_1\rangle$ by numerically finding that $r_{01} = r_{10} = 0$ when $\alpha \approx 0.1546$. We posit the existence of α_{optimal} for larger spin chains, where such an α can be numerically identified, as demonstrated in the 4-site model, by minimizing the vector containing all off-diagonal matrix elements coupling the ground state to higher energy states.

G. Algorithm in 2D

As illustrated in the bottom right panel of Fig. 2, in two dimensions Eq. (35)'s nearest neighbor ($\langle i, j \rangle$) interactions still run over the horizontal ($(i, j), (i \pm 1, j)$) lattice sites, as in the prior 1D case, and now additionally run over the vertical ($(i, j), (i, j \pm 1)$) edges. As illustrated in Fig. 5, the nearest neighbor interaction graph can be partitioned into four (as in 1D, equal to the spin coordination number) components:

$$\hat{A} = \sum_{j=0, i=0}^{j=N-1, i=\frac{N}{2}-1} \hat{H}_{(2i, j), (2i+1, j)}, \quad (65)$$

$$\hat{B} = \sum_{j=0, i=0}^{j=N-1, i=\frac{N}{2}-1} \hat{H}_{(2i+1, j), (2i+2, j)}, \quad (66)$$

$$\hat{C} = \sum_{i=0, j=0}^{i=N-1, j=\frac{N}{2}-1} \hat{H}_{(i, 2j), (i, 2j+1)}, \quad (67)$$

$$\hat{D} = \sum_{i=0, j=0}^{i=N-1, j=\frac{N}{2}-1} \hat{H}_{(i, 2j+1), (i, 2j+1)}. \quad (68)$$

Note that, for a given value of j , \hat{A} and \hat{B} reduce to the one-dimensional case we have already analyzed above. \hat{C} and \hat{D} likewise tile the vertical edges. Subsequently, the scheme to time evolve is similar to the prior 1D case. The only difference is that each spin variable is involved in four interactions as colored. Taken together, this gate sequence constitutes a 2D Trotterized time-evolution clock cycle which is stroboscopically applied until the desired propagation time.

The 2D model's logical displacement operators are

$$D_{\hat{A}}^{(n)} = \prod_{j=0, i=0}^{j=N-1, i=\frac{N}{2}-1} D_{\hat{H}_{(2i, j), (2i+1, j)}}^{(n)}, \quad (69)$$

$$D_{\hat{B}}^{(n)} = \prod_{j=0, i=0}^{j=N-1, i=\frac{N}{2}-1} D_{\hat{H}_{(2i+1, j), (2i+2, j)}}^{(n)}, \quad (70)$$

$$D_{\hat{C}}^{(n)} = \prod_{i=0, j=0}^{i=N-1, j=\frac{N}{2}-1} D_{\hat{H}_{(i, 2j), (i, 2j+1)}}^{(n)}, \quad (71)$$

$$D_{\hat{D}}^{(n)} = \prod_{i=0, j=0}^{i=N-1, j=\frac{N}{2}-1} D_{\hat{H}_{(i, 2j+1), (i, 2j+1)}}^{(n)}. \quad (72)$$

The transversal bosonic SWAP operators, which interchange modes along bonds tiling the 2D lattice, now read

$$T_{\hat{A}} = \bigotimes_{j=0, i=0}^{j=N-1, i=\frac{N}{2}-1} \text{SWAP}^{(2i, j), (2i+1, j)}, \quad (73)$$

$$T_{\hat{B}} = \bigotimes_{j=0, i=0}^{j=N-1, i=\frac{N}{2}-1} \text{SWAP}^{(2i+1, j), (2i+2, j)}, \quad (74)$$

$$T_{\hat{C}} = \bigotimes_{i=0, j=0}^{i=N-1, j=\frac{N}{2}-1} \text{SWAP}^{(i, 2j), (i, 2j+1)}, \quad (75)$$

$$T_{\hat{D}} = \bigotimes_{i=0, j=0}^{i=N-1, j=\frac{N}{2}-1} \text{SWAP}^{(i, 2j+1), (i, 2j+1)}. \quad (76)$$

We define the back-to-back execution of Eqs. (73, 74) and Eqs. (75, 76) as the permutation operators

$$T_{\hat{A}\hat{B}} = T_{\hat{B}} T_{\hat{A}}, \quad (77)$$

$$T_{\hat{C}\hat{D}} = T_{\hat{D}} T_{\hat{C}}. \quad (78)$$

In the case of the 1D algorithm, the subscript on the displacement operator generator Then the SELECT unitary in 2D reads

$$V_{\hat{H}'}^{(2D)}(\alpha) = \prod_{\hat{L} \in \{\hat{A}, \hat{B}, \hat{C}, \hat{D}\}} \left[T_{\hat{C}\hat{D}} (T_{\hat{A}\hat{B}} D_{\hat{L}}(\alpha))^{\frac{N}{2}} \right]^{\frac{N}{2}} \quad (79)$$

$$\begin{aligned}
&= \prod_{p=t}^{N-1} e^{-2i\alpha \hat{D} \otimes \hat{p}_t} \times \prod_{s=0}^{N-1} e^{-2i\alpha \hat{C} \otimes \hat{p}_s} \\
&\times \prod_{q=0}^{N-1} e^{-2i\alpha \hat{B} \otimes \hat{p}_q} \times \prod_{p=0}^{N-1} e^{-2i\alpha \hat{A} \otimes \hat{p}_p}
\end{aligned} \quad (80)$$

This is the desired expression in used in 2D versions of Theorem 3 and Theorem 5. A visual, quantum circuit representation of this algorithm appears in the bottom panel of Fig. 6.

V. PHYSICAL ERROR ANALYSIS

A complete understanding of algorithmic and physical errors together in quantum computations is an open problem. In developing this new framework, we first derived an algorithm where hardware errors were taken to be vanishingly small. While a complete analysis of the effect of physical hardware errors on the Gaussian energy projection protocol is beyond the scope of this work, here we briefly discuss the dominant error processes and their relevance to our oracles.

The important errors to consider in experimental implementation of our Gaussian projection protocol are the (weak) amplitude damping of the oscillators at rate κ , and bit-flip and phase flip errors in the qubits [15]. For short times, δt , the Kraus operators associated with amplitude damping in a given oscillator are

$$K_0 = \sqrt{1 - \kappa \delta t} a^\dagger a \approx e^{-\frac{\kappa}{2} \delta t \hat{a}^\dagger \hat{a}} \quad (81)$$

$$K_1 = \sqrt{\kappa \delta t} \hat{a}. \quad (82)$$

Here K_1 is the photon loss ‘jump operator’ and K_0 is the ‘no-jump’ operator describing the Bayesian update that reduces the amplitude of large photon number states when no photon escapes into the environment [47].

For simplicity, we will analyze the effect of the Kraus operators within the simple model of the protocol given at the beginning of Sec. II in Eqs. (1-2). Interestingly, the no-jump errors associated with K_0 deterministically shrink the coherent amplitudes, but this simply yields a decrease in the effective value of β , so that the only effect is to lower the strength of the projection. If a jump error occurs, the photon loss re-weights the relative amplitudes of the states. In the simplest case of a single photon loss, the (unnormalized) state is approximately given by

$$\begin{aligned}
D_{\hat{H}'}(\beta - \tilde{\beta}) a D_{\hat{H}'}(\tilde{\beta}) |\Psi_{\text{in}}\rangle &= \sum_n \tilde{\beta}_n D_{\hat{H}'}(\beta) |E_n\rangle \otimes |0\rangle \\
&= \sum_n \tilde{\beta}_n \psi_n |E_n\rangle \otimes |\beta_n\rangle, \quad (83)
\end{aligned}$$

where $\tilde{\beta}_n = \tilde{\beta}(E_n - E_s)$ is the value of the oscillator coherent state amplitude at the time of the photon jump part-way through the protocol. Therefore, the resulting state

is identical to $|\Psi_{\text{out}}\rangle$ up to the prefactors $\tilde{\beta}_n$ that rescale the relative weight of each eigenstate $|E_n\rangle$. This rescaling reduces the effectiveness of projection into states with energy eigenvalues near E_s , but is not fatal to the protocol in the sense that eigenstates with energy eigenvalues far from E_s are still strongly projected out.

We note that in writing the above, we have made the simplifying assumption that the protocol can be approximated as a continuous displacement of the qumode at a rate proportional to the spin eigenvalue. In practice, complications can arise from photon loss during the compilation steps needed to produce the weight-2 Pauli strings in the spin Hamiltonian. In particular, photon loss during a conditional displacement or beam splitter gate will manifest similarly to the rescaling effect above; in contrast, photon loss during a controlled parity gate will produce errors that propagate in a more complicated and generally fatal fashion.

Qubit decay and dephasing will produce additional errors which will require modeling, beyond the scope of this work, for quantitative error emulation. One can, however, obtain a sense of the circuit depths that are achievable by considering the relevant time-scales. In current hardware, beam-splitter $\text{BS}^{(j,k)}(\theta, \varphi)$ (e.g., cavity SWAP) gates have durations on the order of ~ 100 ns [14, 48, 49], controlled-parity operations, $P_{Z_k}^{(j)}$, require of order $\sim 1 \mu\text{s}$ [14, 16, 50, 51], and controlled displacements require of order $\sim 0.25 - 1 \mu\text{s}$ [52]. These times are to be compared to state-of-the-art transmon lifetimes of $\sim 300 - 500 \mu\text{s}$ [53, 54], and superconducting resonator lifetimes of $\sim 1 - 1000$ ms [55–59].

Lastly, we outline a protocol to disentangle algorithmic errors from the physical errors appearing due to hardware and control imperfections. To do so, we consider a randomized benchmarking protocol at the oracular level. The main idea in randomized benchmarking of qubit unitaries is to apply ‘typical Haar random’ circuits which are logical identity operators. The circuits should also be representative of the random gate set being benchmarked. The physical errors lead to exponentially decaying observables, with respect to the logical identity’s depth, which are efficient to evaluate. Consequently, randomized benchmarking provides a simple and useful estimate of physical gate errors. RB algorithms addressing bosonic operations have recently appeared [60].

In addition to physical-level RB, one may by using $\text{Tr}_{\mathbf{B}}(|\langle m|U_x(\alpha)|0\rangle|^2) = \sum_{m=0}^{\infty} (\hat{P}_\tau^m)^\dagger \hat{P}_\tau^m = \mathbf{1}_{\mathbf{Q}}$, also consider a logical-level oracular randomized benchmark (ORB). The bold letters denote the composite space of all bosons or qubits. This means that our filters expressed in Eq. (A4) are Kraus operators, each representing a distinct spectral filter, satisfying the above completeness relation. One implication is that, by tracing over all photon numbers, we stochastically apply $\mathbf{1}_{\mathbf{Q}}$. Spectral ORB protocol therefore will measure an important, domain-specific function of an easy-to-prepare input state. The above trace is simply evaluated in a stochastic manner by iteratively sampling over all photon numbers measured.

VI. CONCLUSION

In this work, we explicitly constructed a spectral filter (imaginary-time propagating) that propagates a target quantum system to, for example, a ground state. We partitioned this task into the compilation and application of block-encoded quantum oracles, which take advantage of analog features such as i) the infinite-dimensional support of bosonic field variables and ii) the ease of manipulating Gaussian states. In doing so, our protocol lifts unitary DV circuits to a popular CV-DV architecture, where transmon qubits are interspersed (Fig. 2, [15]) with microwave cavity oscillators.

To develop our framework, we first provided a theory of block encoding functions using both qubit and Gaussian CV variables. These CV-DV operators were then used to compile circuits which approximate desired spectral filter functions, i.e. acting with respect to a parent Hamiltonian. In addition to considering the ideal filter, we have also derived the contributions of algorithmic errors within the block encoding procedure, with both heterodyne detection and photon-based block encodings analyzed. Overall, our framework defines a stochastic process that can be taken as a semi-coherent process [61] with lower coherence requirements or augmented with the use of amplitude amplification as needed.

The middle part of this work was dedicated to synthesizing CV-DV circuits which ε -approximate the Gaussian spectral transformation oracles. We first outlined the gate set, for the base interactions that the Trotter product formula employs, and how these gates are themselves synthesized in terms of physical interactions between qubits and qumodes. Afterwards, we derived the base Trotter factorizations, as well as the associated error scaling, in which imaginary time scaling is a convolution of the real time errors. By analytically and numerically analyzing a minimal example, we optimized the displacement strength and discussed the success probabilities of the protocol. Lastly, we demonstrate that the projection is highly parallelizable for $M = N$ bosonic mode and generalized the spectral filtering algorithm to 2D.

Our work demonstrates how complex oracular functions can be optimally encoded by a judicious selection of physical degrees of freedom and Gaussian CV-DV unitary gates and measurements. Future work may also generalize the class of integral-based, block encoded oracles. In principle, our work can be straightforwardly generalized to simulate non-Heisenberg models. For example, one may examine spin models residing on tri-coordinated lattices or those with next-nearest-neighbor spin interactions.

We note that the hybrid qubit-oscillator operations required for the implementation of our protocol are experimentally feasible with high quality, and have already been demonstrated at small scales [16, 52]. This begs the question of what their role is in the grand scheme of quantum computation. Looking beyond direct implementations in the near term, we note that there are a

variety of ways that our algorithm may be generalized to be compatible with quantum error correction. In addition to qubit-only fault-tolerant implementations, where the continuous field is discretized [20], one may consider a paradigm where, in order to minimize the overall resource cost, error-corrected logical qubits are combined with low-error oscillators. Such an approach is well-suited to the hierarchy of error rates in the proposed hybrid CV-DV architecture, where qubit errors are the dominant source of error [15]. Furthermore, the compilation techniques discussed in this work can be extended to realize controlled displacements conditioned on logical spin operators. That is, given the trade-off between the number and quality of logical qubits encoded from physical qubits, we conjecture that a semi-fault-tolerant paradigm, using high-quality-factor qumodes, can minimize overall resources by maximizing the number and fault tolerance of the encoded logical qubits. In addition, oscillator encodings may also be combined with our framework to partially suppress the noise on the oscillators and the Gaussian gates they utilize [62]. Overall, more research is required to holistically analyze and optimize experimentally available resources.

Finally, we provided a preliminary analysis of physical errors. In particular, we discussed how native error channels both contribute and can be characterized at various algorithmic levels. To quantify these effects, we provided physical error rates and examined their leading order contribution to our target propagator. We then examined the bosonic variants of physical level randomized benchmarking and outlined a logical-level ORB, a variant of randomized benchmarking which naturally emerges by treating all non-vacuum block-encoded operations equally and sampling over all outcomes. Reference 63, which encodes diagrammatically defined operators in terms of the VTA with similar architecture, appeared during the completion of this manuscript.

The data and code that support the findings in this study are available at Ref. 64.

ACKNOWLEDGMENTS

We thank P. Lotshaw for helpful comments. L.B. was supported by DOE ASCR funding under the Quantum Computing Application Teams program, FWP ERKJ347. Y.W. is supported by the U.S. Department of Energy, Office of Science, National Quantum Information Science Research Centers, Quantum Science Center, and DOE ASCR funding under the Accelerated Research in Quantum Computing Program, FWP ERKJ445. E.D. is supported by the U.S. Department of Energy, Office of Science, Advanced Scientific Research Program, Early Career Award under contract number ERKJ420. K.S. was supported by the U.S. Department of Energy, Office of Science, National Quantum Information Science Research Centers, Co-design Center for Quantum Advantage under contract number DE-

SC0012704. Y.L. acknowledges the support by the U.S. Department of Energy, Office of Science, Advanced Scientific Computing Research, under contract number DE-SC0025384. S.M.G. acknowledges additional support for research sponsored by the Army Research Office (ARO), and accomplished under Grant Number W911NF-23-1-0051. The views and conclusions contained in this document are those of the authors and should not be interpreted as representing the official policies, either expressed or implied, of the Army Research Office (ARO), or the U.S. Government. The U.S. Government is authorized to reproduce and distribute reprints for Government purposes notwithstanding any copyright notation herein.

External Interest Disclosure: S.M.G. is a consultant for, and equity holder in, Quantum Circuits, Inc.

Author contributions: YW, YL, ED, and SMG conceptualized initial methodologies. LB, KCS, YL, and SMG developed the instruction set architecture and provided hardware-specific details. LB, KCS, and YW contributed to visualization as well as numerical and analytical validation. KCS, YL, ED, and SMG analyzed physical errors. All authors contributed to original writing, review and editing, and mathematical formulation of the end-to-end compilation presented.

Appendix A: Brief review of continuous variables

First set $\hbar = 1$ (e.g., in the time evolution operator $\exp(-it\hat{H}/\hbar) \rightarrow \exp(-it\hat{H})$). Recall the bosonic field operators for the j^{th} mode create, acting as $\hat{a}_j^\dagger |n\rangle_j = \sqrt{n+1} |n+1\rangle_j$, or annihilate, acting as $\hat{a}_j |n\rangle_j = \sqrt{n} |n-1\rangle_j$, a photon excitation. The field operators are subject to the bosonic commutation relations $[\hat{a}_i, \hat{a}_j^\dagger] = \delta_{i,j}$.

Focusing on a single CV mode, and dropping the mode index, we define the hermitian quadrature operators (analogous dimensionless position and momentum operators)

$$\hat{x} = \lambda_x (\hat{a} + \hat{a}^\dagger), \quad (\text{A1a})$$

$$\hat{p} = -i\lambda_p (\hat{a} - \hat{a}^\dagger), \quad (\text{A1b})$$

where $\lambda_{x,p} \in \mathbb{R}$. The choice of $\lambda_x = \lambda_p = 1/2$ defines Wigner units and corresponds to

$$\hat{a} = \hat{x} + i\hat{p}, \quad (\text{A2a})$$

$$\hat{a}^\dagger = \hat{x} - i\hat{p}. \quad (\text{A2b})$$

It is straightforward to verify $[\hat{x}, \hat{p}] = (i/2)[\hat{a}, \hat{a}^\dagger] = i/2$, which is as if $\hbar = 1/2$ in the canonical commutation relation $[\hat{x}, \hat{p}] = i\hbar$ where \hat{x} and \hat{p} are dimensional position and momentum operators, respectively.

Wigner units subsequently define the width of the momentum-space Gaussian wavefunction for the vacuum state $|0\rangle$ as $\psi_0(p) = \langle p|0\rangle = \langle p|(\int |x\rangle\langle x| dx)|0\rangle =$

$\int \langle p|x\rangle \langle x|0\rangle dx = \int \psi_p^*(x) \psi_0(x) dx = (2/\pi)^{1/4} e^{-p^2}$, where the position space vacuum wavefunction in Wigner units is $\psi_0(x) = \langle x|0\rangle = (2/\pi)^{1/4} e^{-x^2}$ [15] and the plane-wave function $\psi_p(x) = \langle x|p\rangle = \pi^{-1/2} e^{2ipx}$ [$\pi^{-1/2}$ factor so that orthogonality reads $\langle p|p'\rangle = \int \psi_p(x) \psi_{p'}^*(x) dx = \delta(p - p')$]. In this way, Eq. (17) has the physical interpretation of being the expectation value of the operation $U_{\hat{H}'}^{(\hat{p})}(\alpha) = e^{-2i\alpha\hat{H}' \otimes \hat{p}}$, with respect to the cavity electromagnetic field's vacuum state $|0\rangle$.

Eq. (17) is derived by setting $K \rightarrow \pm\tau\hat{H}'$ in the expression for the position boosted state in Eq. 36 of Ref. 15, multiplying by $\langle p|0\rangle$ and integrating over position coordinates. That is the same as setting $\hat{A} = iK = \pm i\tau\hat{H}'$ in Eq. (6). As a result of Wigner units, and the factor of two coming with $i\alpha$, the “expectation value” (an operator in fact) of the position displacement conditioned on the principal system's Hamiltonian, $\langle 0|U_{\hat{H}'}^{(\hat{p})}(\alpha)|0\rangle = \int dp \langle 0|p\rangle U_{\hat{H}'}^{(p)}(\alpha) \langle p|0\rangle$, becomes

$$\begin{aligned} &= \sqrt{\frac{2}{\pi}} \int dp e^{-2p^2} e^{-2i\alpha\hat{H}'p} \\ &= \sqrt{\frac{2}{\pi}} \int dp e^{-2(p^2\mathbb{1} + i\alpha p\hat{H}')} \\ &= \sqrt{\frac{2}{\pi}} \int dp e^{-2(p\mathbb{1} + i\frac{\alpha}{2}\hat{H}')^2 + 2(i\frac{\alpha}{2}\hat{H}')^2} \\ &= e^{2(i\frac{\alpha}{2}\hat{H}')^2} = e^{-(\alpha\hat{H}')^2/2} = \hat{P}_{\hat{H}'}(\alpha). \end{aligned} \quad (\text{A3})$$

For the interested reader, note that Equation (12) indicates $e^{i\theta}D(\alpha)$ forms a group (Heisenberg group) with a geometric phase $e^{i(\text{Re } \alpha)(\text{Im } \alpha)}$, where $(\text{Re } \alpha)(\text{Im } \alpha)$ is twice the area enclosed by vectors $z_1 = i \text{Im } \alpha$, $z_2 = \text{Re } \alpha$, and $z_3 = -\alpha$ in the complex plane. In addition, any complex displacement $D(\alpha)$ can be factorized into a momentum boost $D(i \text{Im } \alpha)$ followed by a position displacement $D(\text{Re } \alpha)$, together with a geometric phase [15].

Last, we calculate the m -photon wavefunction in momentum basis $\psi_m(p) = \langle p|m\rangle$ that is used in the Sec. II C. Using $|m\rangle = \frac{1}{\sqrt{m!}}(\hat{a}^\dagger)^m |0\rangle$ and $\hat{a}^\dagger = \hat{x} - i\hat{p} = e^{\hat{p}^2} \hat{x} e^{-\hat{p}^2}$ [65] and plugging in $\hat{x} \rightarrow \frac{i}{2}\partial_p$, we have $\psi_m(p) = \langle p|m\rangle = \frac{1}{\sqrt{m!}} \langle p|e^{\hat{p}^2} \hat{x}^m e^{-\hat{p}^2}|0\rangle = \frac{1}{\sqrt{m!}} [e^{p^2} (\frac{i}{2}\partial_p)^m (e^{-p^2} \langle p|0\rangle)] = \frac{(-i)^m}{\sqrt{2^m m!}} \psi_0(p) H_m(\sqrt{2}p)$, where $\langle p|0\rangle = \psi_0(p) = (2/\pi)^{1/4} e^{-p^2}$, $H_m(p) = (-1)^m e^{p^2} (\partial_p)^m e^{-p^2} = (2p - \partial_p)^m \cdot 1$ is the m th Hermite polynomial.

Alternatively, a simplified proof of Eq. (18) goes as follows [similar to the derivation to Eq. (38) in Ref. 33]. Denoting $\hat{\xi} = \tau\hat{H}'$ and using $U_{\hat{H}'}^{(\hat{p})}(\tau) = e^{-i\tau\hat{H}'\hat{p}} = e^{\hat{\xi}\hat{a}^\dagger - \hat{\xi}\hat{a}} = e^{-\hat{\xi}^2/2} e^{\hat{\xi}\hat{a}^\dagger} e^{-\hat{\xi}\hat{a}}$ and $\hat{a}^m e^{\hat{\xi}\hat{a}^\dagger} = (\hat{a} + \hat{\xi})^m$, we find the matrix element

$$\hat{P}_{\hat{H}'}(m, \tau) = \langle m|U_{\hat{H}'}^{(\hat{p})}(\tau)|0\rangle$$

$$\begin{aligned}
&= \frac{1}{\sqrt{m!}} \langle 0 | \hat{a}^m e^{\hat{\xi} \hat{a}^\dagger - \hat{\xi} \hat{a}} | 0 \rangle \\
&= \frac{e^{-\hat{\xi}^2/2}}{\sqrt{m!}} \langle 0 | e^{\hat{\xi} \hat{a}^\dagger} (\hat{a} + \hat{\xi})^m e^{-\hat{\xi} \hat{a}} | 0 \rangle \\
&= \frac{e^{-\hat{\xi}^2/2}}{\sqrt{m!}} \langle 0 | (\hat{a} + \hat{\xi})^m | 0 \rangle \\
&= \frac{e^{-\hat{\xi}^2/2} \hat{\xi}^m}{\sqrt{m!}} = \frac{(\tau \hat{H}')^m}{\sqrt{m!}} e^{-\frac{\tau^2}{2} \hat{H}'^2}. \quad (\text{A4})
\end{aligned}$$

Appendix B: Proof of Theorem 5

We give a brief proof of Eqs. (46) to (48) in Theorem 5. After expressing the LTHS operator $\hat{R}_{\hat{H}}(\alpha) = \langle 0 | \cdot | 0 \rangle$ in the integral form $\int d\mathbf{p} \langle 0 | \cdot | \mathbf{p} \rangle \langle \mathbf{p} | 0 \rangle / \pi^M$ (in Wigner units) and using the vacuum wavefunction in the momentum basis $\psi_0(\mathbf{p}) = \langle \mathbf{p} | 0 \rangle = (2\pi)^{M/4} e^{-\mathbf{p} \cdot \mathbf{p}} = (2\pi)^{M/4} \prod_{j=0}^{M-1} e^{-p_j^2}$, Eq. (46a) becomes

$$(2/\pi)^{\frac{M}{2}} \int d\mathbf{p} \prod_{\gamma=1}^{\Gamma} \prod_{j=0}^{M-1} e^{-2p_j^2} e^{-2i(\alpha/\sqrt{M}) \hat{H}_{\gamma} p_j} \quad (\text{B1})$$

$$= (2/\pi)^{\frac{M}{2}} \int d\mathbf{p} \mathcal{T}_{\gamma} \prod_{j=0}^{M-1} e^{-2p_j^2 - 2i(\alpha/\sqrt{M}) (\sum_{\gamma} \hat{H}_{\gamma}) p_j} \quad (\text{B2})$$

$$= \mathcal{T}_{\gamma} \prod_{j=0}^{M-1} \sqrt{2/\pi} \int dp_j e^{-2p_j^2 - 2i(\alpha/\sqrt{M}) (\sum_{\gamma} \hat{H}_{\gamma}) p_j} \quad (\text{B3})$$

$$= \mathcal{T}_{\gamma} \prod_{j=0}^{M-1} e^{-\alpha^2 (\sum_{\gamma} \hat{H}_{\gamma})^2 / (2M)} \quad (\text{B4})$$

$$= \mathcal{T}_{\gamma} e^{-\alpha^2 (\sum_{\gamma} \hat{H}_{\gamma})^2 / 2}. \quad (\text{B5})$$

This gives Eq. (46b).

To prove Eq. (47) we again apply the HS transformation with a variable k to $\hat{P}_{\hat{H}}$ and $\hat{R}_{\hat{H}}$ respectively:

$$\hat{P}_{\hat{H}}(\alpha) = \sqrt{\frac{2}{\pi}} \int dk e^{-2k^2} e^{-2i\alpha \hat{H} k}, \quad (\text{B6a})$$

$$\begin{aligned}
\hat{R}_{\hat{H}}(\alpha) &= \mathcal{T}_{\gamma} \sqrt{\frac{2}{\pi}} \int dk e^{-2k^2} e^{-2i\alpha (\sum_{\gamma} \hat{H}_{\gamma}) k} \\
&= \sqrt{\frac{2}{\pi}} \int dk e^{-2k^2} \prod_{\gamma=1}^{\Gamma} e^{-2i\alpha \hat{H}_{\gamma} k}. \quad (\text{B6b})
\end{aligned}$$

As shown by the integral form Eq. (B6b), the LTHS synthesized $\hat{R}_{\hat{H}}(\alpha)$ operator by displacing M oscillators with α/\sqrt{M} in parallel is identical to the LTHS synthesized operator by displacing a single oscillator with α , given our choice of parallel gate sequences (a different choice may result numerically similar LTHS approximation for $\hat{R}_{\hat{H}}$ but more complicated analytical expression).

Using triangle inequality for integrals, we have

$$\begin{aligned}
&\left\| \hat{R}_{\hat{H}}(\alpha) - \hat{P}_{\hat{H}}(\alpha) \right\| \\
&\leq \sqrt{\frac{2}{\pi}} \int dk e^{-2k^2} \left\| \prod_{\gamma=1}^{\Gamma} e^{-2i\alpha \hat{H}_{\gamma} k} - e^{-2i\alpha (\sum_{\gamma} \hat{H}_{\gamma}) k} \right\| \\
&\leq \sqrt{\frac{2}{\pi}} \int dk e^{-2k^2} 2\alpha^2 k^2 \sum_{\gamma_1=1}^{\Gamma} \left\| \sum_{\gamma_2=\gamma_1+1}^{\Gamma} [H_{\gamma_2}, H_{\gamma_1}] \right\| \quad (\text{B7}) \\
&\leq \frac{\alpha^2}{2} \sum_{\gamma_1 < \gamma_2} \| [H_{\gamma_1}, H_{\gamma_2}] \|.
\end{aligned}$$

In Eq. (B7) we used the Proposition 9 from Ref. 41.

Finally, to obtain Eq. (48) for Heisenberg interactions, we begin with the integral form Eq. (B6b). First, by definition, each $\hat{H}_{\gamma} = \sum_{\delta=1}^{\Delta_{\gamma}} \hat{H}_{\gamma,\delta}$ consists of mutually commuting Heisenberg coupling bonds $\hat{H}_{\gamma,\delta} = X_{j_1} X_{j_2} + Y_{j_1} Y_{j_2} + Z_{j_1} Z_{j_2}$, where the qubit indices (j_1, j_2) are uniquely determined by the indices (γ, δ) and $\delta \in \{1, \dots, \Delta_{\gamma}\}$ labels the edges of the same color indexed by γ . $\hat{H}_{\gamma,\delta}$ has the eigenvalue $+1$ (-3) on the local triplet (singlet) subspace $\text{span}\{|00\rangle, |11\rangle, |01\rangle + |10\rangle\}$ ($\text{span}\{|01\rangle - |10\rangle\}$), resulting in the triplet (singlet) projector $\pi_{\gamma,\delta}^0 = (3 + \hat{H}_{\gamma,\delta})/4$ and $\pi_{\gamma,\delta}^1 = (1 - \hat{H}_{\gamma,\delta})/4$. Since the projectors are idempotent, $(\pi_{\gamma,\delta}^0)^2 = \pi_{\gamma,\delta}^0$ and $(\pi_{\gamma,\delta}^1)^2 = \pi_{\gamma,\delta}^1$, and orthogonal, $\pi_{\gamma,\delta}^0 \pi_{\gamma,\delta}^1 = 0$, the exponential factor $e^{-2i\alpha k \hat{H}_{\gamma}} = \prod_{\delta=1}^{\Delta_{\gamma}} e^{-2i\alpha k \hat{H}_{\gamma,\delta}} = \prod_{\delta=1}^{\Delta_{\gamma}} e^{-2i\alpha k (\pi_{\gamma,\delta}^0 - 3\pi_{\gamma,\delta}^1)} = \prod_{\delta=1}^{\Delta_{\gamma}} (e^{-2i\alpha k} \pi_{\gamma,\delta}^0 + e^{6i\alpha k} \pi_{\gamma,\delta}^1)$, which can then be expanded as homogeneous polynomial of degree Δ_{γ} . Thus, with an explicit constant spectrum shift $\sum_{\gamma} \hat{H}_{\gamma} \rightarrow (\sum_{\gamma} \hat{H}_{\gamma}) - E_s$, Eq. (B6b) becomes

$$\begin{aligned}
&\sqrt{\frac{2}{\pi}} \int dk e^{-2k^2 + 2i\alpha E_s k} \prod_{\gamma=1}^{\Gamma} \prod_{\delta=1}^{\Delta_{\gamma}} (e^{-2i\alpha k} \pi_{\gamma,\delta}^0 + e^{6i\alpha k} \pi_{\gamma,\delta}^1) \\
&= \sum_{\{b_{\gamma,\delta}\} \in \{0,1\}^{|E(G)|}} w(\alpha; \{b_{\gamma,\delta}\}) \prod_{\gamma=1}^{\Gamma} \prod_{\delta=1}^{\Delta_{\gamma}} \pi_{\gamma,\delta}^{b_{\gamma,\delta}}, \quad (\text{B8})
\end{aligned}$$

where the sum runs through all $|E(G)|$ bit-variables $b_{\gamma,\delta}$ [one for each edge of Heisenberg interaction graph $G = (V, E)$] and the Gaussian weight factors

$$\begin{aligned}
&w(\alpha; \{b_{\gamma,\delta}\}) \\
&= \sqrt{\frac{2}{\pi}} \int dk e^{-2k^2 + 2i\alpha E_s k + \sum_{\gamma,\delta} [6i\alpha k b_{\gamma,\delta} - 2i\alpha k (1 - b_{\gamma,\delta})]} \\
&= e^{-\alpha^2 [E_s + \sum_{\gamma,\delta} (4b_{\gamma,\delta} - 1)]^2 / 2}. \quad (\text{B9})
\end{aligned}$$

Considering the indices $(\gamma, \delta) \leftrightarrow (j_1, j_2)$ labeling the same set of edges with Heisenberg interactions, and the explicitly color-ordered product \prod_{γ} can be indicated with color ordering operator \mathcal{T}_{γ} , the Eqs. (B8) and (B9) prove the Eq. (48).

Appendix C: Analytical Results for 1D Chain

For 1D chain colored as in Fig. 5(a), we write out the specific analytical forms for $\hat{R}_{\hat{H}}(\alpha)$ given by Eqs. (B8) and (B9) [equivalently, Eq. (48)].

For an even N -site chain with periodic boundary condition, label the N sites $0, 1, \dots, N-1$ and color the edges $\{(2j, 2j+1)\}_{j=0}^{N/2-1}$ red and the edges $\{(2j+1, 2j+2)\}_{j=0}^{N/2-1}$ blue (index N also labels the site 0), as shown in Fig. 5(a). Using Eqs. (B8) and (B9), we find

$$\hat{R}_{\hat{H}}(\alpha) = \sum_{\mathbf{b} \in \{0,1\}^N} e^{-\alpha^2(E_s - N + 4 \sum_{j=0}^{N-1} b_j)^2/2} \times \left(\prod_{j=0}^{\frac{N}{2}-1} \pi_{2j+1, 2j+2}^{b_{j+\frac{N}{2}}} \right) \left(\prod_{j=0}^{\frac{N}{2}-1} \pi_{2j, 2j+1}^{b_j} \right). \quad (\text{C1})$$

Here, the bit-variables define a vector $\mathbf{b} = (b_0, b_1, \dots, b_{N-1}) \in \{0, 1\}^N$ and, equivalently, a bit string $b = b_{N-1} \dots b_1 b_0 \in \{0, \dots, 2^N - 1\}$.

For $N = 4$, Eq. (C1) becomes

$$\hat{R}_{\hat{H}}(\alpha) = \sum_{\mathbf{b} \in \{0,1\}^4} e^{-\alpha^2(E_s - 4 + 4 \sum_j b_j)^2/2} \pi_{3,0}^{b_3} \pi_{1,2}^{b_2} \pi_{2,3}^{b_1} \pi_{0,1}^{b_0}. \quad (\text{C2})$$

Since we use the 4-site example to illustrate our algorithm, it is desirable to have more detailed analytical result in energy eigenbasis $\{|E_n\rangle\}_{n=0}^{16}$ so that the eigenstate projection action by the LTHS operator $\hat{R}_{\hat{H}'}(\alpha)$, where $\hat{H}' = \hat{H} - E_s$, can be understood more easily with respect to the parameters α and E_s . For all degeneracies, it is sufficient to use simultaneous eigenstates for the following conserved symmetry (i.e., commuting with \hat{H}) operators ($\mathbf{S}^2, \mathbf{S}_z, \text{SWAP}_{1,3}$), where $\mathbf{S}_z = \sum_j Z_j/2$, $\mathbf{S}^2 = \mathbf{S}_x^2 + \mathbf{S}_y^2 + \mathbf{S}_z^2$, and $\text{SWAP}_{1,3} = (\hat{H}_{1,3} + \mathbb{1})/2$.

In this energy eigenbasis listed in Table II, Eq. (C2) becomes

$$\begin{aligned} \hat{R}_{\hat{H}'}(\alpha) = & \sum_{i,j \in \{0,4\}} g_{i,j}(\alpha; E_s) |E_i\rangle\langle E_j| \\ & + g_t(\alpha; E_s) \sum_{k=1}^3 |E_k\rangle\langle E_k| \\ & + g_s(\alpha; E_s) \sum_{k=5}^{10} |E_k\rangle\langle E_k| \\ & + g_q(\alpha; E_s) \sum_{k=11}^{15} |E_k\rangle\langle E_k|. \end{aligned} \quad (\text{C3})$$

where g_t, g_s, g_q are weights for the triple-, sextuple-, and quintuple-rank projectors, and the expressions for these

n	E_n	s	s_z	$\sigma_{1,3}$
0	-8	0	0	1
1	-4	1	-1	1
2	-4	1	0	1
3	-4	1	1	1
4	0	0	0	-1
5	0	1	-1	-1
6	0	1	-1	1
7	0	1	0	-1
8	0	1	0	1
9	0	1	1	-1
10	0	1	1	1
11	4	2	-2	1
12	4	2	-1	1
13	4	2	0	1
14	4	2	1	1
15	4	2	2	1

TABLE II. Eigenbasis for 4-site Heisenberg chain, labeled by energies and conserved quantum numbers ($s, s_z, \sigma_{1,3}$) corresponding to total \mathbf{S} , total \mathbf{S}_z , and parity under $\text{SWAP}_{1,3}$ (symmetry with respect to the mirror axis connecting site 0 and 2).

weights are:

$$g_{00} = \frac{-e_0 + 6e_2 + 3e_4}{8}, \quad (\text{C4a})$$

$$g_{44} = \frac{3e_0 + 6e_2 - e_4}{8}, \quad (\text{C4b})$$

$$g_{04} = \frac{\sqrt{3}(e_0 - 2e_2 + e_4)}{8}, \quad (\text{C4c})$$

$$g_{40} = -g_{04}, \quad (\text{C4d})$$

$$g_t = e_2, \quad g_s = \frac{e_1}{2}, \quad g_q = e_0, \quad (\text{C4e})$$

where

$$e_k = e^{-\alpha^2(E_s - 4 + 4k)^2/2}, \quad k \in \{0, 1, 2, 3\}. \quad (\text{C4f})$$

Note that $g_{04} < 0, \forall \alpha \neq 0$ [66]. So for any finite α , the excited state $|E_4\rangle$ will be mixed in the projection of ground state $|E_0\rangle$ regardless of the choice of E_s or α . From the symmetry point of view, the highlighted eigenstates $|E_0\rangle$ and $|E_4\rangle$ in Table II have the same spin symmetry $s = s_z = 0$ despite large energy difference, so $|E_4\rangle$ is usually not fully filtered out by $\hat{R}_{\hat{H}'}(\alpha)$ operator that preserves the spin symmetry. One solution is to apply a projector $\frac{1}{2}(\text{SWAP}_{1,3} + \mathbb{1}) = \frac{1}{4}(\hat{H}_{1,3} + 3)$ to select the ground state with even symmetry $\sigma_{1,3} = +1$.

However, for infinitesimal α , it is easy to verify that

$$\hat{R}_{\hat{H}'}(\alpha)$$

$$= \sum_{k=0}^{15} \left[1 - \alpha^2 (E_k - E_s)^2 / 2 \right] |E_k\rangle\langle E_k| + \mathcal{O}(\alpha^4) \quad (\text{C5})$$

$$= \sum_{k=0}^{15} e^{-\alpha^2 (E_k - E_s)^2 / 2} |E_k\rangle\langle E_k| + \mathcal{O}(\alpha^4) \quad (\text{C6})$$

$$= \hat{P}_{\hat{H}'}(\alpha) + \mathcal{O}(\alpha^4), \quad (\text{C7})$$

where $\hat{P}_{\hat{H}'}(\alpha)$ is the exact ground state projector for a shift $E_s = E_0$. Thus, the LTHS is always a valid ground (eigen-) state filter with controllable error for small α .

Appendix D: Visual Compilations for 6-site Heisenberg Chain

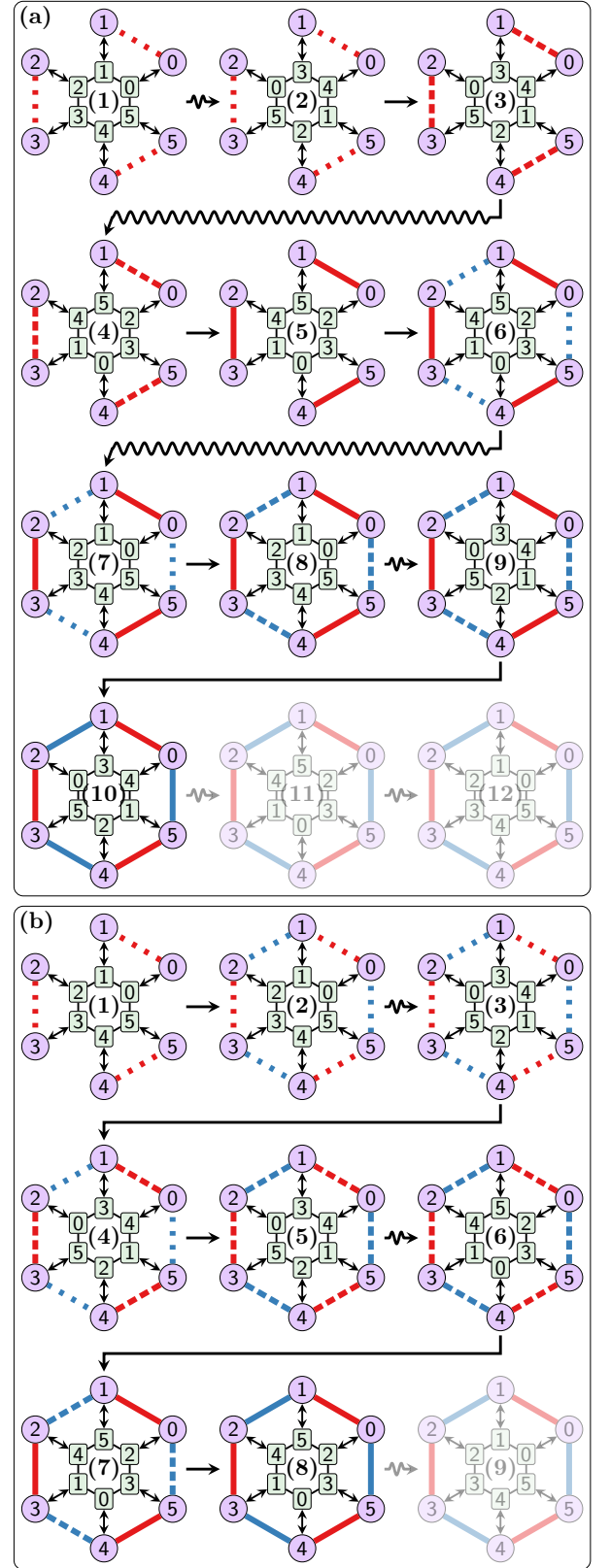


FIG. 10. Visual representations of the compilations for $N = 6$ site Heisenberg model. See Fig. 7 caption for notations.

- [1] A. Gilyén, Y. Su, G. H. Low, and N. Wiebe, Quantum singular value transformation and beyond: exponential improvements for quantum matrix arithmetics, in *Proceedings of the 51st Annual ACM SIGACT Symposium on Theory of Computing*, STOC 2019 (Association for Computing Machinery, New York, NY, USA, 2019) pp. 193–204, [arXiv:1806.01838 \[quant-ph\]](#).
- [2] J. M. Martyn, Z. M. Rossi, A. K. Tan, and I. L. Chuang, Grand unification of quantum algorithms, *PRX Quantum* **2**, 040203 (2021).
- [3] R. Irmejs, M. C. Bañuls, and J. I. Cirac, Efficient quantum algorithm for filtering product states, *Quantum* **8**, 1389 (2024).
- [4] A. Litteken, L. M. Seifert, J. D. Chadwick, N. Nottingham, T. Roy, Z. Li, D. Schuster, F. T. Chong, and J. M. Baker, Dancing the quantum waltz: Compiling three-qubit gates on four level architectures, in *Proceedings of the 50th Annual International Symposium on Computer Architecture*, ISCA '23 (Association for Computing Machinery, New York, NY, USA, 2023).
- [5] N. C. Menicucci, S. T. Flammia, and O. Pfister, One-way quantum computing in the optical frequency comb, *Phys. Rev. Lett.* **101**, 130501 (2008).
- [6] A. Sørensen and K. Mølmer, Quantum computation with ions in thermal motion, *Phys. Rev. Lett.* **82**, 1971 (1999).
- [7] E. A. Martinez, C. A. Muschik, P. Schindler, D. Nigg, A. Erhard, M. Heyl, P. Hauke, M. Dalmonte, T. Monz, P. Zoller, and R. Blatt, Real-time dynamics of lattice gauge theories with a few-qubit quantum computer, *Nature* **534**, 516–519 (2016).
- [8] O. Katz, L. Feng, A. Risinger, C. Monroe, and M. Cetina, Demonstration of three- and four-body interactions between trapped-ion spins, *Nature Physics* **19**, 1452 (2023).
- [9] Z. Davoudi, N. M. Linke, and G. Pagano, Toward simulating quantum field theories with controlled phonon-ion dynamics: A hybrid analog-digital approach, *Physical Review Research* **3**, 10.1103/physrevresearch.3.043072 (2021).
- [10] E. Crane, K. C. Smith, T. Tomesh, A. Eickbusch, J. M. Martyn, S. Kühn, L. Funcke, M. A. DeMarco, I. L. Chuang, N. Wiebe, A. Schuckert, and S. M. Girvin, Hybrid oscillator-qubit quantum processors: Simulating fermions, bosons, and gauge fields (2024), [arXiv:2409.03747 \[quant-ph\]](#).
- [11] N. Liu, J. Thompson, C. Weedbrook, S. Lloyd, V. Vedral, M. Gu, and K. Modi, Power of one qumode for quantum computation, *Phys. Rev. A* **93**, 052304 (2016).
- [12] D.-B. Zhang, G.-Q. Zhang, Z.-Y. Xue, S.-L. Zhu, and Z. D. Wang, Continuous-variable assisted thermal quantum simulation, *Phys. Rev. Lett.* **127**, 020502 (2021).
- [13] J. D. Teoh, P. Winkel, H. K. Babla, B. J. Chapman, J. Claes, S. J. de Graaf, J. W. O. Garmon, W. D. Kalfus, Y. Lu, A. Maiti, K. Sahay, N. Thakur, T. Tsunoda, S. H. Xue, L. Frunzio, S. M. Girvin, S. Puri, and R. J. Schoelkopf, Dual-rail encoding with superconducting cavities, *Proc. Natl. Acad. Sci.* **120**, e2221736120 (2023).
- [14] K. S. Chou, T. Shemma, H. McCarrick, T.-C. Chien, J. D. Teoh, P. Winkel, A. Anderson, J. Chen, J. C. Curtis, S. J. de Graaf, J. W. O. Garmon, B. Gudlewski, W. D. Kalfus, T. Keen, N. Khedkar, C. U. Lei, G. Liu, P. Lu, Y. Lu, A. Maiti, L. Mastalli-Kelly, N. Mehta, S. O. Mundhada, A. Narla, T. Noh, T. Tsunoda, S. H. Xue, J. O. Yuan, L. Frunzio, J. Aumentado, S. Puri, S. M. Girvin, S. H. Moseley, and R. J. Schoelkopf, A superconducting dual-rail cavity qubit with erasure-detected logical measurements, *Nat. Phys.* **20**, 1454 (2024).
- [15] Y. Liu, S. Singh, K. C. Smith, E. Crane, J. M. Martyn, A. Eickbusch, A. Schuckert, R. D. Li, J. Sinanan-Singh, M. B. Soley, T. Tsunoda, I. L. Chuang, N. Wiebe, and S. M. Girvin, Hybrid oscillator-qubit quantum processors: Instruction set architectures, abstract machine models, and applications (2024), [arXiv:2407.10381 \[quant-ph\]](#).
- [16] C. S. Wang, J. C. Curtis, B. J. Lester, Y. Zhang, Y. Y. Gao, J. Freeze, V. S. Batista, P. H. Vaccaro, I. L. Chuang, L. Frunzio, L. Jiang, S. M. Girvin, and R. J. Schoelkopf, Efficient multiphoton sampling of molecular vibronic spectra on a superconducting bosonic processor, *Phys. Rev. X* **10**, 021060 (2020).
- [17] C. S. Wang, N. E. Frattini, B. J. Chapman, S. Puri, S. M. Girvin, M. H. Devoret, and R. J. Schoelkopf, Observation of wave-packet branching through an engineered conical intersection, [arXiv:2202.02364](#) (2022).
- [18] The method can be applied to degenerate ground states with some small adaptation.
- [19] L. Lin and Y. Tong, Near-optimal ground state preparation, *Quantum* **4**, 372 (2020).
- [20] T. Keen, E. Dumitrescu, and Y. Wang, Quantum algorithms for ground-state preparation and green's function calculation (2021), [arXiv:2112.05731 \[quant-ph\]](#).
- [21] A. M. Childs and N. Wiebe, Hamiltonian simulation using linear combinations of unitary operations, *Quantum Info. Comput.* **12**, 901 (2012).
- [22] Y. Ge, J. Tura, and J. I. Cirac, Faster ground state preparation and high-precision ground energy estimation with fewer qubits, *J. Math. Phys.* **60**, 022202 (2019).
- [23] M. Motta, C. Sun, A. T. K. Tan, M. J. O'Rourke, E. Ye, A. J. Minnich, F. G. S. L. Brandão, and G. K.-L. Chan, Determining eigenstates and thermal states on a quantum computer using quantum imaginary time evolution, *Nat. Phys.* **16**, 205 (2020).
- [24] J. C. Getelina, N. Gomes, T. Iadecola, P. P. Orth, and Y.-X. Yao, Adaptive variational quantum minimally entangled typical thermal states for finite temperature simulations, *SciPost Physics* **15**, 10.21468/scipostphys.15.3.102 (2023).
- [25] D. Camps and R. Van Beeumen, FABLE: Fast approximate quantum circuits for block-encodings, in *2022 IEEE International Conference on Quantum Computing and Engineering (QCE)* (2022) pp. 104–113.
- [26] P. Kuklinski and B. Rempfer, S-FABLE and LS-FABLE: Fast approximate block-encoding algorithms for unstructured sparse matrices (2024), [arXiv:2401.04234 \[quant-ph\]](#).
- [27] D. Camps, L. Lin, R. Van Beeumen, and C. Yang, Explicit quantum circuits for block encodings of certain sparse matrices, *SIAM J. Matrix Anal. Appl.* **45**, 801 (2024).
- [28] J. Sinanan-Singh, G. L. Mintzer, I. L. Chuang, and Y. Liu, Single-shot quantum signal processing interferometry (2023), [arXiv:2311.13703 \[quant-ph\]](#).

- [29] Z. M. Rossi, V. M. Bastidas, W. J. Munro, and I. L. Chuang, [Quantum signal processing with continuous variables](#) (2023).
- [30] The CCR indicates that unbounded CV operators cannot reside in a finite dimensional Hilbert space [67, 68] like qubit systems. Suppose such a trace were well defined. Then $\text{Tr}([\hat{x}, \hat{p}]) = \text{Tr}(\hat{x}\hat{p}) - \text{Tr}(\hat{p}\hat{x}) = 0$ by the cyclic property, which contradicts the CCR.
- [31] The eigenvectors corresponding to these eigenvalues live in a rigged (meaning equipped) Hilbert space so the spectrum need not be quantized (or countable).
- [32] Ref. 69 being an inspirational *exception* to this trend.
- [33] R. P. Feynman, An operator calculus having applications in quantum electrodynamics, [Phys. Rev. **84**, 108 \(1951\)](#).
- [34] T. A. Besselova and O. Kyriienko, Hamiltonian operator approximation for energy measurement and ground-state preparation, [PRX Quantum **2**, 10.1103/prxquantum.2.030318 \(2021\)](#).
- [35] Strictly speaking, the Rodrigues formula in Eq. (18) defines the complex Itô-Hermite polynomial basis $H_{m,n}(z, z^*)$.
- [36] G. H. Low and I. L. Chuang, Hamiltonian simulation by qubitization, [Quantum **3**, 163 \(2019\)](#).
- [37] U. Chabaud, T. Douce, F. Grosshans, E. Kashefi, and D. Markham, Building trust for continuous variable quantum states (2019), [arXiv:1905.12700 \[quant-ph\]](#).
- [38] C. S. Jackson, The photodetector, the heterodyne instrument, and the principle of instrument autonomy (2022), [arXiv:2210.11100 \[quant-ph\]](#).
- [39] C. S. Jackson and C. M. Caves, How to perform the coherent measurement of a curved phase space by continuous isotropic measurement. I. Spin and the Kraus-operator geometry of $\text{SL}(2, \mathbb{C})$, [Quantum **7**, 1085 \(2023\)](#).
- [40] This SWAP definition follows Eq. (188) of Ref. [15]. Alternatively, following Eq. (286) of Ref. [15] we can define $\text{SWAP}^{(j,k)} := \text{BS}^{(j,k)}(\pi, \frac{\pi}{2})\Pi^{(k)}$ where the photon number parity gate $\Pi^{(k)} = [F^{(k)}]^2 = (-1)^{\hat{n}_k}$, which is less symmetric with respect to index $j \leftrightarrow k$.
- [41] A. M. Childs, Y. Su, M. C. Tran, N. Wiebe, and S. Zhu, Theory of Trotter error with commutator scaling, [Phys. Rev. X **11**, 011020 \(2021\)](#).
- [42] C. Kang, M. B. Soley, E. Crane, S. Girvin, and N. Wiebe, Leveraging hamiltonian simulation techniques to compile operations on bosonic devices, [arXiv preprint arXiv:2303.15542 \(2023\)](#).
- [43] A. Carrera Vazquez, D. J. Egger, D. Ochsner, and S. Woerner, Well-conditioned multi-product formulas for hardware-friendly Hamiltonian simulation, [Quantum **7**, 1067 \(2023\)](#).
- [44] P. K. Faehrmann, M. Steudtner, R. Kueng, M. Kieferova, and J. Eisert, Randomizing multi-product formulas for Hamiltonian simulation, [Quantum **6**, 806 \(2022\)](#).
- [45] S. Zhuk, N. Robertson, and S. Bravyi, Trotter error bounds and dynamic multi-product formulas for Hamiltonian simulation (2023), [arXiv:2306.12569 \[quant-ph\]](#).
- [46] More explicitly, \hat{R}_α is block diagonal in the simultaneous eigenbasis of \hat{H}_4 and its mutually commuting symmetry operators $\{\hat{S}_{\text{tot}}^2, \hat{S}_Z, \hat{\sigma}_{24}\}$ where $\hat{\sigma}_{24} = \frac{1}{2}(\mathbb{1} + X_2X_4 + Y_2Y_4 + Z_2Z_4)$ is a swap operator between sites 2 and 4.
- [47] M. H. Michael, M. Silveri, R. T. Brierley, V. V. Albert, J. Salmilehto, L. Jiang, and S. M. Girvin, New class of quantum error-correcting codes for a bosonic mode, [Phys. Rev. X **6**, 031006 \(2016\)](#).
- [48] B. J. Chapman, S. J. de Graaf, S. H. Xue, Y. Zhang, J. Teoh, J. C. Curtis, T. Tsunoda, A. Eickbusch, A. P. Read, A. Koottandavida, S. O. Mundhada, L. Frunzio, M. H. Devoret, S. M. Girvin, and R. J. Schoelkopf, High-on-off-ratio beam-splitter interaction for gates on bosonically encoded qubits, [PRX Quantum **4**, 020355 \(2023\)](#).
- [49] Y. Lu, A. Maiti, J. W. O. Garmon, S. Ganjam, Y. Zhang, J. Claes, L. Frunzio, S. M. Girvin, and R. J. Schoelkopf, High-fidelity parametric beamsplitting with a parity-protected converter, [Nature Communications **14**, 5767 \(2023\)](#).
- [50] L. Sun, A. Petrenko, Z. Leghtas, B. Vlastakis, G. Kirchmair, K. M. Sliwa, A. Narla, M. Hatridge, S. Shankar, J. Blumoff, L. Frunzio, M. Mirrahimi, M. H. Devoret, and R. J. Schoelkopf, Tracking photon jumps with repeated quantum non-demolition parity measurements, [Nature **511**, 444 \(2014\)](#).
- [51] S. J. de Graaf, S. H. Xue, B. J. Chapman, J. D. Teoh, T. Tsunoda, P. Winkel, J. W. Garmon, K. M. Chang, L. Frunzio, S. Puri, *et al.*, A mid-circuit erasure check on a dual-rail cavity qubit using the joint-photon number-splitting regime of circuit qed, [arXiv:2406.14621 \(2024\)](#).
- [52] A. Eickbusch, V. Sivak, A. Z. Ding, S. S. Elder, S. R. Jha, J. Venkatraman, B. Royer, S. M. Girvin, R. J. Schoelkopf, and M. H. Devoret, Fast universal control of an oscillator with weak dispersive coupling to a qubit, [Nature Physics **10**, 1038/s41567-022-01776-9 \(2022\)](#).
- [53] A. P. M. Place, L. V. H. Rodgers, P. Mundada, B. M. Smitham, M. Fitzpatrick, Z. Leng, A. Premkumar, J. Bryon, A. Vrajitoarea, S. Sussman, G. Cheng, T. Madhavan, H. K. Babla, X. H. Le, Y. Gang, B. Jäck, A. Geynis, N. Yao, R. J. Cava, N. P. de Leon, and A. A. Houck, New material platform for superconducting transmon qubits with coherence times exceeding 0.3 milliseconds, [Nature Communications **12**, 1779 \(2021\)](#).
- [54] C. Wang, X. Li, H. Xu, Z. Li, J. Wang, Z. Yang, Z. Mi, X. Liang, T. Su, C. Yang, G. Wang, W. Wang, Y. Li, M. Chen, C. Li, K. Linghu, J. Han, Y. Zhang, Y. Feng, Y. Song, T. Ma, J. Zhang, R. Wang, P. Zhao, W. Liu, G. Xue, Y. Jin, and H. Yu, Towards practical quantum computers: transmon qubit with a lifetime approaching 0.5 milliseconds, [npj Quantum Information **8**, 3 \(2022\)](#).
- [55] M. Reagor, W. Pfaff, C. Axline, R. W. Heeres, N. Ofek, K. Sliwa, E. Holland, C. Wang, J. Blumoff, K. Chou, M. J. Hatridge, L. Frunzio, M. H. Devoret, L. Jiang, and R. J. Schoelkopf, Quantum memory with millisecond coherence in circuit QED, [Physical Review B **94**, 014506 \(2016\)](#).
- [56] A. Romanenko, R. Pilipenko, S. Zorzetzi, D. Frolov, M. Awida, S. Belomestnykh, S. Posen, and A. Grassellino, Three-dimensional superconducting resonators at $t < 20$ mK with photon lifetimes up to $\tau = 2$ s, [Physical Review Applied **13**, 034032 \(2020\)](#).
- [57] O. Milul, B. Guttel, U. Goldblatt, S. Hazanov, L. M. Joshi, D. Chausovsky, N. Kahn, E. Çiftçürek, F. Lafont, and S. Rosenblum, A superconducting quantum memory with tens of milliseconds coherence time, [PRX Quantum **4**, 030336 \(2023\)](#).
- [58] S. Ganjam, Y. Wang, Y. Lu, A. Banerjee, C. U. Lei, L. Krayzman, K. Kisslinger, C. Zhou, R. Li, Y. Jia, M. Liu, L. Frunzio, and R. J. Schoelkopf, Surpassing millisecond coherence in on chip superconducting quantum memories by optimizing materials and circuit design, [Na-](#)

- ture Communications **15**, 3687 (2024).
- [59] I. Pietikäinen, O. c. v. Černotík, A. Eickbusch, A. Maiti, J. W. Garmon, R. Filip, and S. M. Girvin, Strategies and trade-offs for controllability and memory time of ultra-high-quality microwave cavities in circuit quantum electrodynamics, *PRX Quantum* **5**, 040307 (2024).
 - [60] C. H. Valahu, T. Navickas, M. J. Biercuk, and T. R. Tan, Benchmarking bosonic modes for quantum information with randomized displacements, *arXiv preprint arXiv:2405.15237* (2024).
 - [61] Y. Wang, S. Chehade, and E. Dumitrescu, Semicoherent symmetric quantum processes: Theory and applications, *AVS Quantum Science* **6**, 10.1116/5.0215919 (2024).
 - [62] K. Noh, S. M. Girvin, and L. Jiang, Encoding an oscillator into many oscillators, *Phys. Rev. Lett.* **125**, 080503 (2020).
 - [63] S. Varona, S. Saner, O. B. azāvan, G. Araneda, G. Aarts, and A. Bermudez, Towards quantum computing feynman diagrams in hybrid qubit-oscillator devices (2024), *arXiv:2411.05092*.
 - [64] L. Bell, Trotter Scaling Bounds (2025), <https://github.com/luke-d-bell/trotter-scaling-bounds>.
 - [65] This can be proved by using the so-called Hadamard lemma (Campbell identity) $e^A B e^{-A} = B + [A, B] + \frac{1}{2!}[A, [A, B]] + \frac{1}{3!}[A, [A, [A, B]]] + \dots$. Note that a nonunitary transformation is applied to transform a Hermitian operator \hat{x} to a non-Hermitian one \hat{a}^\dagger .
 - [66] Jensen's inequality can be used to show $g_{04} < 0$, that is, $(e_0 + e_4)/2 < e_2$ as follows: $\forall \alpha \neq 0$, $(e_0 + e_4)/2 = [e^{-\alpha^2(E_s-4)^2/2} + e^{-\alpha^2(E_s+12)^2/2}]/2 < e^{-\alpha^2[(E_s-4)^2+(E_s+12)^2]/4} \leq e^{-\alpha^2[(E_s+4)^2]/2} = e_2$.
 - [67] F. Gieres, Mathematical surprises and Dirac's formalism in quantum mechanics, *Rep. Prog. Phys.* **63**, 1893 (2000), Example 1.
 - [68] H. Weyl, *The Theory of Groups and Quantum Mechanics*, 2nd ed. (Dover, 1931), p95.
 - [69] Y. Chen and T.-C. Wei, Quantum algorithm for spectral projection by measuring an ancilla iteratively, *Phys. Rev. A* **101**, 032339 (2020).